Planetary and Space Science 71 (2012) 80–100

Contents lists available at SciVerse ScienceDirect

Planetary and Space Science

journal homepage: www.elsevier.com/locate/pss

Selecting the geology filter wavelengths for the ExoMars Panoramic Camera instrument

Claire R. Cousins [a,b,*], Matthew Gunn [c], Bryan J. Prosser [e], Dave P. Barnes [g], Ian A. Crawford [a,b], Andrew D. Griffiths [b,d], Lottie E. Davis [b,f], Andrew J. Coates [b,d]

[a] Department of Earth and Planetary Sciences, Birkbeck College, University of London, Malet Street, WC1E 7HX, UK
[b] Centre for Planetary Sciences at UCL/Birkbeck, Gower Street, London, WC1E 6BT, UK
[c] Institute for Mathematics and Physics, Aberystwyth University, Aberystwyth, SY23 3BZ, UK
[d] Mullard Space Science Laboratory, University College London, Holmbury St. Mary, Dorking, RH5 6NT, UK
[e] Department of Computer Science, Queen Mary, University of London, E1 4NS, UK
[f] Department of Earth Sciences, University College London, Gower Street, WC1E 6BT, UK
[g] Department of Computer Science, Aberystwyth University, Aberystwyth, SY23 2AX, UK

ARTICLE INFO

Article history:
Received 9 January 2012
Received in revised form
8 May 2012
Accepted 9 July 2012
Available online 20 July 2012

Keywords:
ExoMars
Mars
PanCam
Hydrated minerals
Reflectance spectroscopy

ABSTRACT

The Panoramic Camera (PanCam) instrument will provide surface remote sensing data for the ExoMars mission. A combination of wide-angle stereo, multispectral, and high resolution imagery will generate contextual geological information to help inform which scientific targets should be selected for drilling and analysis. One component of the PanCam dataset is narrowband multispectral imaging in the visible to near infrared, which utilises a dedicated set of 12 "geology" filters of predetermined wavelength and bandwidth to view the terrain, and provide information on composition and putative mineralogy. The centre wavelengths and bandwidths of these filters were optimised to account for the highly diverse mineralogical terrains the ExoMars rover will hopefully encounter. Six new alternative test filter sets were created, each optimised for the detection of either: sulfates, phyllosilicates, ferric oxides, mafic silicates, iron absorptions, and minor hydration absorptions. These six filter sets were cross-tested using database mineral reflectance spectra and Mars analogue rock multispectral data to find the best performing filter set. Once selected, the bandwidths of this filter set were also optimised. The filter set optimised to ferric oxide minerals was able to most accurately represent rock multispectral data, as well as capture subtle spectral features of hydrated minerals, including sulfates, phyllosilicates, and carbonates. These filters differ from those used on past missions (e.g., Pathfinder, Mars Exploration Rover) and represent the next evolutionary stage in PanCam instrument development. When compared to past filter sets, the updated ExoMars filters capture rock and mineral spectral data more effectively, enhancing the ability of the ExoMars PanCam to detect lithological and compositional variation within an outcrop.

1. Introduction

1.1. The ExoMars Panoramic Camera

The ExoMars mission, and in particular rock or outcrop target selection, will be heavily dependent upon data from the Panoramic Camera (PanCam) instrument. PanCam has numerous science objectives (Griffiths et al., 2006), one of which – the assessment of the geological terrain proximal to the rover – will be crucial for identifying drilling targets, and providing the geological (and therefore palaeoenvironmental) context to any sample analysis undertaken. In addition, assessment of the local geology will generate scientific findings in its own right, as seen with the Mars Exploration Rover (MER) Pancam (e.g., Bell et al., 2004; Farrand et al., 2006, 2008; Johnson et al., 2007; Schmidt et al., 2009; Rice et al., 2010). The PanCam for ExoMars will consist of 2 wide angle cameras (WACs) with a 34° field of view (FoV), separated by a distance of 50 cm; and a single High Resolution Camera with a narrow FoV of 4°. The WACs each have a filter wheel to allow both narrowband multispectral imaging and broadband colour imaging. For a detailed instrument description see Griffiths et al. (2006). PanCam science for ExoMars will be achieved with a combination of wide-angle stereo colour panoramas and 3D digital elevation models (DEM), high resolution colour images/mosaics, reflectance spectra of Regions of Interest (ROI) and 2D mapping of spectral features (e.g., band depth).

Multispectral imaging in particular is achieved via a dedicated "geology" filter set consisting of narrowband filters of pre-determined wavelengths between 440 and 1000 nm, placed in front of the wide-angle camera lens via a filter wheel (Fig. 1). There are 22 filters in total, distributed across 2 filter wheels, 12 of which are assigned

* Corresponding author. Tel.: +44 20 7679 7986.
E-mail address: c.cousins@ucl.ac.uk (C.R. Cousins).

0032-0633/$ - see front matter © 2012 Elsevier Ltd. All rights reserved.
http://dx.doi.org/10.1016/j.pss.2012.07.009

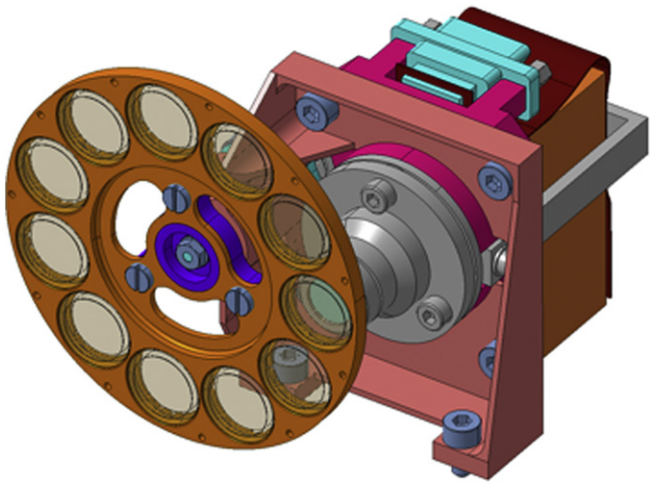

Fig. 1. ExoMars PanCam design showing the position of the filter wheel in front of the Wide Angle Camera lens. Credit: Craig Theobald.

specifically to providing narrowband multispectral data of the geological terrain. These 12 filters can be used to generate coarse reflectance spectra to identify putative mineralogy and composition of a rock or soil target, as well as providing 2D spatial multispectral data to enable mapping of spectrally distinct (and therefore potentially lithologically distinct) units within an outcrop (e.g., Farrand et al., 2006, 2007, 2008; Rice et al., 2010). The centre wavelengths of the geology filters for other Martian missions are summarised in Cousins et al. (2010).

PanCam multispectral imaging is scientifically limited in its capacity to provide visible to near infrared (Vis–NIR) spectral data by the utilisation of a silicon detector, which is only sensitive to wavelengths between ~400 and 1000 nm. The vast majority of reflectance spectral features (i.e., absorption bands) occur at wavelengths >1 μm, and are therefore missed by PanCam. However, the multispectral capability of PanCam can still be exploited, firstly to capture those spectral features that do exist <1 μm, and secondly to provide information of spectral variability within a terrain which can be spatially related to structural units and lithological heterogeneity (e.g., see Farrand et al., 2008). The two-dimensional nature of the data allows spectral features and differences, however minor, to be mapped and related to observable geological features seen in the images. The application of PanCam multispectral data therefore is two-fold: first to provide the initial *tentative* identification of broad mineralogical species present in the surface rocks, and second to map the spectral diversity and features within a scene (even if spectra cannot be readily assigned to a known mineral).

For these applications to be successful, the geological filters need to capture effectively the spectral shape of a wide variety of minerals potentially present at the Martian surface. Any spectral absorptions or features missed could lead to misleading results, such as the mis-identification of a mineralogical/compositional or spectral unit. The limitation of PanCam to sample the Vis–NIR wavelength range at 12 individual wavelengths only (due to engineering constraints) can therefore be mitigated by selecting wavelengths that best capture the spectral morphology of minerals and rocks. Table 1 lists mineral species identified on Mars, together with their absorption features within the PanCam spectral range. Some minerals, such as calcite, albite, and magnesite are largely featureless at these wavelengths.

1.2. Multispectral geology filters

Geology filter wavelengths were first conceived for the Imager for Mars Pathfinder on the 1997 NASA Pathfinder mission (Smith et al., 1997a, b), and surface/Panoramic camera instruments for subsequent Mars rover missions have largely inherited these geology filter wavelengths (MER, Beagle 2, and Phoenix: Bell et al., 2003; Griffiths et al., 2005; Lemmon et al., 2008, respectively). The Pathfinder geological filters were, as with many Pathfinder technologies, the first of their kind. They were selected with the aim to identify and discriminate between iron-bearing minerals, including iron oxides and iron silicates, particularly different pyroxenes (Smith et al., 1997a, b). For the MER Pancam, these filters were largely adopted, with the exception of the 965 nm filter which was omitted. The scientific rationale for using the same filter wavelengths was to allow for the direct comparison of MER results to those acquired from Pathfinder (Bell et al., 2003). Likewise, the Pathfinder filters were again adopted for the Beagle 2 PanCam (Griffiths et al., 2005). ExoMars however has a distinct astrobiological focus, and it will be especially important to locate the most likely outcrops to search for biosignatures. It is also noted that the "geology" filter wavelengths for the MastCam instrument (Ghaemi, 2009) on the NASA Mars Science Laboratory (MSL) rover are also different to those of past missions, by reducing the number of filters in the visible. However, the scientific rationale for this has not so far been published.

Since Pathfinder there has been a multitude of orbital (e.g., CRISM, OMEGA) and in situ (MER) data detailing the mineralogy of the Martian surface (Chevrier and Mathe, 2007; Murchie et al., 2009). This information has shown Mars to be mineralogically diverse, with an apparently complex geological history preserving a number of different palaeoenvironmental conditions (Bibring et al., 2006; Bishop et al., 2008; Ehlmann et al., 2008b, 2011; Poulet et al., 2005; Wray et al., 2009; Weitz et al., 2011). In particular, the discovery of hydrated mineral terrains has demonstrated the possibility for past "habitable" conditions on Mars, which are of direct relevance to the ExoMars mission. Given that the Pathfinder filters were devised over a decade ago, coupled with the advancing knowledge of Mars surface mineralogy, the ExoMars filters represent the next evolutionary stage in filter wavelength selection.

This work sought to find the 12 best filter wavelengths for the ExoMars PanCam, based on the greatly improved knowledge of mineralogical terrains on Mars. Preliminary work by Cousins et al. (2010) demonstrated the need to revise the filter wavelengths for ExoMars objectives, especially in the detection of hydrated minerals and astrobiological targets. During this previous investigation, no work was carried out to determine the effect of filter bandwidth on the measured reflectance spectra. For this reason, the effect of bandwidth on measured data has been assessed and optimum bandwidths determined.

2. Materials & methods

Selecting the new geology filter wavelengths utilised reflectance spectral data of hydrated minerals, mafic rock forming silicates, and iron oxides. The aim was to find the 12 filter wavelengths that could most accurately reproduce the spectra of different minerals relevant to the astrobiological focus of the ExoMars mission, as well as be able to detect other minerals likely to found at the Martian surface. Table 2 summarises the considerations regarding selecting filters based upon mineral species. It is also noted that UV-induced fluorescence is also being developed as an additional technique to multispectral PanCam imaging (Storrie-Lombardi et al., 2009), and this too is in-part reliant on the narrowband geology filter wavelengths selected (Dartnell et al., 2010).

2.1. Filter centre wavelength optimisation

Six new alternative filter sets (consisting of 12 filters each between 440 and 1000 nm) were created utilising mineral reflectance

Table 1
Minerals identified on Mars as detected by oribital TES, CRISM, and OMEGA instruments (e.g., Bibring et al., 2007; Bishop et al., 2008; Ehlmann et al., 2008a, 2009; Farrand et al., 2009; Gendrin et al., 2005; Langevin et al., 2005; Loizeau et al., 2007; Michalski and Niles 2010; Milam et al. 2010; Milliken et al., 2008; Osterloo et al., 2008; Poulet et al., 2005; Mustard et al., 2008; Wray et al., 2009), and in-situ Pathfinder/MER/Phoenix instruments (e.g., Boynton et al., 2009; Hecht et al., 2009; Morris et al., 2000, 2006; Squyres et al., 2004; Squyres et al., 2008). Also see Murchie et al. (2009) and Chevrier and Mathe (2007) for reviews on Martian mineralogy. Minerals used for filter selection are marked ●; minerals used for testing filter sets (either as part of a heterogeneous rock, or as database mineral spectra) are marked†.

Mineral group	Mineral species	Formula	Spectral features (440–1000 nm)
Phyllosilicates	Chlorite ● †	$(Mg,Fe^{2+})_5Al(Si_3Al)O_{10}(OH)_8$	700, 900
	Illite	$(K,H_3O)(Al,Mg,Fe)_2(Si,Al)_4O_{10}[(OH)_2,H_2O$	720, 1000
	Kaolin group minerals	$Al_2Si_2O_5(OH)_4$	1000
	Montmorillonite ● †	$(Na,Ca)_{0.33}(Al,Mg)_2(Si_4O_{10})(OH)_2$	950
	Muscovite	$KAl_2AlSi_3O_{10}(OH)_2$	500
	Nontronite ● †	$(Ca, Na)_{0.3-0.5}(Fe,Mg, Al)_{2-3}(Si, Al)_4O_{10}(OH)_2$	(500), 650, 950
	Saponite ● †	$Ca_{0.25}(Mg,Fe)_3((Si,Al)_4O_{10})(OH)_2 \cdot n(H_2O)$	950
	Serpentine	$(Mg, Fe)_3Si_2O_5(OH)_4$	700, 900
Other hydrated silicates	Prehnite	$Ca_2Al(AlSi_3O_{10})(OH)_2$	–
	Analcime (zeolite) †	$NaAlSi_2O_6\ H_2O$	970
	Opaline silica †	$SiO_2\ H_2O$	(950)
Carbonates	Magnesite †	$MgCO_3$	–
	Calcium carbonate †	$CaCO_3$	–
	Siderite ● †	$FeCO_3$	(500), 650, 900
Sulfates	Fe/Mg poly- hydrated sulfates ● †	$(Fe,Mg)SO_4 \cdot nH_2O$	980
	Gypsum ● †	$CaSO_4 \cdot 2H_2O$	1000
	Alunite ● †	$KAl_3(SO_4)_2(OH)_6$	1000
	Jarosite ● †	$KFe_3(SO_4)_2(OH)_6$	520, 630, 900
	Copiapite ● †	$Fe^{2+}Fe_4^{3+}(SO_4)_6\ (OH)_2 \cdot 20H_2O$	580, 860
Chlorides	Chlorides	–	1000
Perchlorates	Perchlorates	$(Mg,Ca)(ClO_4)_2$	1000
Fe Oxides	Hematite ● †	Fe_2O_3	550, 650, 880 nm
	Goethite ● †	$FeO(OH)$	500, 650, 900 nm
	Ferrihydrite ● †	$5Fe_2O_3 \cdot 9H_2O$	900 nm
	Magnetite ● †	Fe_3O_4	–
	Palagonite/nanophase Fe oxides †	–	–
Mafic silicates	Olivine ● †	$(Mg,Fe)_2SiO_4$	620, 1000
	(high Ca pyroxene)Clinopyroxene ● †	$MgCaSi_2O_6$ (*Diopside*)$(Ca,Na)(Mg,Fe,Al)(Si,Al)_2O_6$ (*Augite*)	800, 1000
	Orthopyroxene ● † (low Ca pyroxene)	$(Mg,Fe)SiO_3$	900
	Plagioclase ● † (albite)	$NaAlSi_3O_8$	–
	Plagioclase † (anorthite)	$CaAl_2Si_2O_8$	–

Table 2
Factors affecting mineral selection for the determination and testing of alternative "geology" filters for the ExoMars PanCam.

Mineral group	Relation to Mars	Spectral features (440–1000 nm)	Drawbacks for filter selection	Solution
Phyllosilicates	Clay-rich sediments preserve organics (Ehlmann et al., 2008b) and are suggestive of past habitable environments, particularly those that were of a neutral-alkaline pH and relatively long-lived (Poulet et al., 2005).	Fe-absorptions in iron-bearing phyllosilicates (e.g., nontronite, chlorite), H_2O/OH^- absorptions in other phyllosilicates (e.g., saponite)	H_2O/OH^- absorptions are weak, and potentially weaker/ non-existent on the drier Martian surface.	Use for filter selection, but be mindful hydration bands shouldn't be relied upon
Sulfates	Sulfate minerals preserve organics (Aubrey et al., 2006), and are associated with a wide-range of geological processes including hydrothermal activity and evaporates.	Strong Fe-absorptions in iron-bearing sulphates (e.g., jarosite, copiapite), and stronger hydration bands than the phyllosilicates (e.g., gypsum, polyhydrated magnesium sulphates)	Sulphates are not always indicative of habitable environments, and therefore may not be the best astrobiological targets for ExoMars.	Use for filter selection
Carbonates and opal	High priority targets due to association with neutral-alkaline aqueous environments, hydrothermal processes, and high preservation potential of biosignatures (e.g., Allen et al., 2000).	Iron-bearing carbonate siderite has strong Fe-absorptions.	No distinctive absorption features within PanCam range for all carbonates (except siderite)	Broad spectral shape suggests any reasonably-spaced filter set will re-produce an accurate spectrum, and therefore will not be used to influence filter wavelengths
Mafic silicates	Mars is predominantly basaltic (McSween et al., 2009), and mafic rock-forming minerals are widespread (Bandfield, 2002).	Strong absorptions in olivine and pyroxene, and distinctive spectral morphologies.	Whilst mafic silicates are likely to be widespread, they are not necessarily applicable to the life detection focus of ExoMars	Use for filter selection due to strong spectral features, but detection of mafic silicates shouldn't take priority
Ferric oxides	Ferric oxides are widespread on Mars, and have the strongest spectral features within the PanCam range. Additionally, iron oxides have been shown to preserve filamentous bacteria (Preston et al., 2011)	Fe^{3+} absorptions in most ferric oxides, with the exception of magnetite which has a comparably featureless spectrum	Ferric oxides are not the most interesting targets for ExoMars	Use for filter selection

spectral datasets acquired from the NASA RELAB facility at Brown University (investigators below), JPL (Baldridge et al., 2009), and USGS (Clark et al., 2007, 1993) online spectral libraries. RELAB data were acquired by Carle M Pieters (CMP, Brown University), Edward A Cloutis (EAC, University of Winnipeg), Jack Mustard (JFM, Brown University), Janice L Bishop (JLB, SETI Institute), Phoebe L. Hauff (PLH, Spectral Research), Roger G Burns (RGB, MIT), Sue Gaffey (SJG), Thomas G Sharp (TGS, Arizona State University), (TJM), Takahiro Hiroi (TXH, Brown University), and Vladimir Busarev (VVB, Moscow University).

Four of these alternative filter sets were each optimised to a specific mineral group, e.g., the best filter set for sulfate minerals ("SULF"), the best for phyllosilicates ("PHYL") etc. In addition, two other filter sets were created optimised to actual absorption features—one for those minerals with Fe^{2+}/Fe^{3+} absorptions, and a second for those minerals with hydration absorptions (OH^-, H_2O). The mineral input data used for each of these six filter sets are given in Table 3, and the mean ($n=8$) spectra of each of these minerals are shown Fig. 2.

Optimal filter centre wavelengths were calculated in Matlab using the method previously devised by Cousins et al. (2010). Briefly, a brute force algorithm was employed to identify the combination of 12 filters (with two filters fixed at 440 and 1000 nm) that reproduced a set of mineral spectra (Fig. 2) with the least amount of error. This method benefits from being non-subjective, and selects filters based on actual mineral spectral data. Input data used for filter selection consisted of reflectance spectra samples ($n=8$) of each mineral species used within a mineral data set (see Table 3). The reflectance data were sub-sampled to 10 nm intervals—the same intervals used for filter assignment. In total, over 29 billion combinations of filters were searched by the programme before the optimum filter wavelengths were found for a given set of mineral input data.

The error with which a set of filters would reproduce a spectrum was measured as an error score. A database mineral reflectance spectrum was sampled at each filter wavelength and then intermediate data points were calculated using linear interpolation. The error score (σ_m) for that mineral was calculated by summing the absolute difference between the original reflectance spectrum and the interpolated reflectance spectrum, using the following equation:

$$\sigma_m = \frac{1}{N} \times \sum_{\lambda=440}^{1000} \left| R_m(\lambda) - R_e(\lambda) \right| \quad (1)$$

where $R_m(\lambda)$ is the reflectance of mineral m at wavelength λ, $R_e(\lambda)$ is the sampled and interpolated reflectance at wavelength λ and N is the number of data points (57 in the case of 10 nm intervals). This is then repeated for each mineral in the dataset, and the resulting error scores for all minerals averaged to obtain a mean

Table 3
Input mineral data for the selection of the six alternative filter sets, from the USGS, RELAB, and JPL spectral databases (see text for references and PI initials). Individual spectra of these are given in Supplementary Material 1.

Filter set	Mineral	RELAB, JPL, and USGS database sample numbers
Group specific minerals		
SULF	Gypsum	HS333; SU2202; SO-2Bb; SO-2Bc; CC-JFM-016-B; SF-BFJ-003; CC-JFM-036; PG-CMP-003
	Alunite	GDS82; GDS84; HS295; SO-4Aa; SO-4Ab; SO-4Ac; CC-JFM-008-B; CC-JFM-009-B
	Jarosite	GDS100; GDS101; GDS24; GDS98; GDS99; JR2501; SJ-1; C1CY16
	Copiapite	CC-JFM-013; JB-JLB-620-A; SF-EAC-052-A; SF-EAC-031-A; LH-JFM-043; PC-RGB-030; GDS21
	Magnesium sulfate	CC-JFM-015; KIEDE1a; KIEDE1b; GDS149; Epsomite; Epsomite2; Hexahydrite1; SF-EAC-056
PHYL	Chlorite	CL-TXH-014; CY-PLH-006; SR-JFM-068; HS197; PS-12A_Medium; PS-12C_Medium; PS-12E_Coarse; PS-12_Fine
	Nontronite	NG-1a; NG-1b; Swa-1a; Swa-1b; PS-6Ba; PS-6Bb; PS-6Da; PS-6Bc
	Montmorillonite	CM26; CM27; Saz-1; Sca-2a; Sca-2b; STx-1; Swy-1; PS-2B
	Saponite	JB-JLB-260; SA-EAC-057; SA-EAC-058; SA-EAC-059; SA-TXH; 051; JM-TGS-075; PS24A_Fine; SapCa1
MAFIC	Olivine	GDS71a; GDS71b; KI3005; KI3054; KI3189; KI3291; KI4143; NMNH137044
	CPX	JB-JLB-471; PA-RGB-024; IN15A; PA-CMP-011; PD-CMP-008; HS15; NMNH18685; IN9B_Coarse
	OPX	JB-JLB-236; PP-EAC-047A; PP-EAC-047B; PP-EAC-052; JB-JLB-238; PP-EAC-013; PP-EAC-043; PP-EAC-057
	Albite	GDS30; HS66; HS143; HS324; PA-CMP-005-C; SR-JFM-047; TS6A_Coarse; TS6A_medium
FERRIC	Hematite	CC-JFM-017; CY-PLH-011; JA-JLB-257; JC-JLB-129; GDS27; HS45; WS161
	Goethite	CY-PLH-008; GO-TXH-001; HO-EAC-003; JB-CMP-047; GDS134; MPCMA2b; WS222; OH-02A_Fine
	Magnetite	FE-RGB-003; JA-JLB-307; JB-JLB-307; MG-EAC-002; MG-EAC-004; PM-CMP-012; SC-EAC-025
	Ferrihydrite	GDS75; JB-CMP-045; JB-JLB-564; JB-JLB-251; JB-JLB-252; JB-JLB-253; JB-JLB-254; JB-JLB-255
All Fe-absorption minerals		
All_Fe	Jarosite	GDS100; GDS101; GDS24; GDS98; GDS99; JR2501; SJ-1; C1CY16
	Copiapite	CC-JFM-013; JB-JLB-620-A; SF-EAC-052-A; SF-EAC-031-A; LH-JFM-043; PC-RGB-030; GDS21
	Chlorite	CL-TXH-014; CY-PLH-006; SR-JFM-068; HS197; PS-12A_Medium; PS-12C_Medium; PS-12E_Coarse; PS-12_Fine
	Nontronite	NG-1a; NG-1b; Swa-1a; Swa-1b; PS-6Ba; PS-6Bb; PS-6Da; PS-6Bc
	Saponite	JB-JLB-260; SA-EAC-057; SA-EAC-058; SA-EAC-059; SA-TXH; 051; JM-TGS-075; PS24A_Fine; SapCa1
	Siderite	CB-EAC-008-A; CB-EAC-008-B; CC-JFM-007-B; CY-PLH-024; GR-CMP-003; JB-JLB-287; SH-SJG-005; C-9A
	Olivine	GDS71a; GDS71b; KI3005; KI3054; KI3189; KI3291; KI4143; NMNH137044
	CPX	JB-JLB-471; PA-RGB-024; IN15A; PA-CMP-011; PD-CMP-008; HS15; NMNH18685; IN9B_Coarse
	OPX	JB-JLB-236; PP-EAC-047A; PP-EAC-047B; PP-EAC-052; JB-JLB-238; PP-EAC-013; PP-EAC-043; PP-EAC-057
	Hematite	CC-JFM-017; CY-PLH-011; JA-JLB-257; JC-JLB-129; GDS27; HS45; WS161
	Goethite	CY-PLH-008; GO-TXH-001; HO-EAC-003; JB-CMP-047; GDS134; MPCMA2b; WS222; OH-02A_Fine
	Magnetite	FE-RGB-003; JA-JLB-307; JB-JLB-307; MG-EAC-002; MG-EAC-004; PM-CMP-012; SC-EAC-025
	Ferrihydrite	GDS75; JB-CMP-045; JB-JLB-564; JB-JLB-251; JB-JLB-252; JB-JLB-253; JB-JLB-254; JB-JLB-255
All hydration absorption minerals		
HYDRA	Gypsum	HS333; SU2202; SO-2Bb; SO-2Bc; CC-JFM-016-B; SF-BFJ-003; CC-JFM-036; PG-CMP-003
	Alunite	GDS82; GDS84; HS295; SO-4Aa; SO-4Ab; SO-4Ac; CC-JFM-008-B; CC-JFM-009-B
	Magnesium sulfate	CC-JFM-015; KIEDE1a; KIEDE1b; GDS149; Epsomite; Epsomite2; Hexahydrite1; SF-EAC-056
	Montmorillonite	CM26; CM27; Saz-1; Sca-2a; Sca-2b; STx-1; Swy-1; PS-2B
	Saponite	JB-JLB-260; SA-EAC-057; SA-EAC-058; SA-EAC-059; SA-TXH; 051; JM-TGS-075; PS24A_Fine; SapCa1

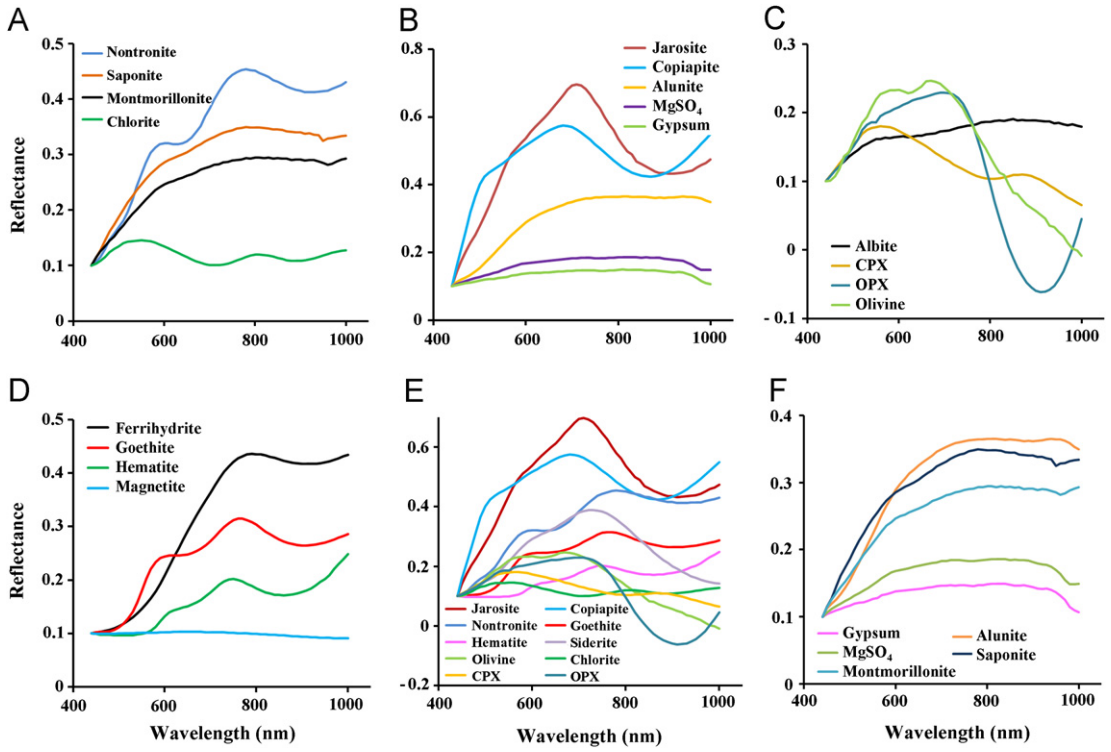

Fig. 2. Mean ($n=8$) reflectance spectra of the minerals used for the selection of filter wavelengths in each of the 6 alternative filter sets: (A) PHYL; (B) SULF; (C) MAFIC; (D) FERRIC; (E) ALL_Fe and (F) HYDRA.

error score (σ) for each filter set:

$$\sigma = \frac{1}{M}\sum_{m=0}^{M-1} \sigma_m \quad (2)$$

where M is the total number of mineral reflectance spectra in the dataset.

2.2. Filter testing and assessment

2.2.1. Test samples

The six alternative filter sets were tested on both the database mineral reflectance data (Table 3), and also on regions of interest (ROI) within Mars analogue geological samples to evaluate their ability to detect mineral targets within an unprocessed, heterogenous rock surface. Geological samples (Fig. 3) are sourced from Iceland, Kenya, and the Department of Earth Sciences geology collections at University College London. The samples contain a variety of sulfate, iron oxide, zeolite, carbonate, smectite/palagonite, and mafic minerals. These geological samples were left untreated/unprocessed so as to represent a natural rock or outcrop surface. A brief description of these samples is as follows (unless stated, all are from Iceland):

- NBO: Acid-weathered basaltic lava with jarosite deposits within vesicles and on the surface (Cousins et al., 2010).
- NAL: Acid-weathered basaltic lava with jarosite, sulphur, and haematite on the surface (Cousins et al., 2010).
- MAG: Magnesite (magnesium carbonate) sample from the UCL Earth Science Geology Collections.
- SKAFTA: Amygdaloidal basalt with vesicle infillings of quartz, clinoptilolite (zeolite), and haematite.
- HYALO: Palagonite-rich hyaloclastite with clasts of basaltic scoria.
- KH: Hyaloclastite with surface (1–3 mm) coating of opaline silica (Cousins et al., 2010).
- GY2: Silica sinter deposit, preserving filamentous biomat textures (Cousins et al., 2010).
- TRONA: sample of trona (sodium carbonate) from Kenya.
- XEN: crushed mantle xenolith rich in olivine and with accessory spinel and pyroxene (Weider et al., 2011). Grain-size <1 mm.
- KRAF: pahoehoe lava with hydrothermal deposits of haematite, sulphur and zeolites.
- HH: Fine-grained buff-coloured hyalotuff, with small $\sim$1 mm basaltic clasts (Cousins et al., 2010).

The majority of samples are from volcanic environments and result from the hydrothermal alteration of basaltic lavas and volcaniclastic deposits. The exceptions are the sample TRONA, which is from an evaporitic environment, and samples XEN and MAG. To confirm mineralogical composition and Vis–NIR reflectance spectra, the ROIs on the rock surface were analysed with Vis–NIR reflectance spectroscopy, Raman spectroscopy, and/or X-ray diffraction (XRD) following multispectral imaging of the samples. This contextual analysis was conducted at Aberystwyth University, using a Bruker D8 Advance XRD with a Vantec 1 detector, Ocean Optics Jaz spectrometer with an ISP-REF integrating sphere probe (used in 8° incident/total hemispherical reflectance geometry) with a fibre coupled external lamp, and a Horiba Jobin Yvon LabRam HR Raman spectrometer with a 632.8 nm laser. Additional Raman spectra were acquired at University College London using a Renishaw InVia Raman Spectrometer with a 785 nm laser.

In addition to the geological samples and mineral data, soil/mixture samples available from the RELAB spectral database (see Section 2.1 above for PI initials) were also used (Fig. 4):

- XT-CMP-030 (25% olivine, 75% bronzite)
- XT-CMP-012 (50% calcite, 50% chlorite)
- MX-EAC-018 (60% pyroxene, 40% haematite)
- MX-EAC-002 (80% pyroxene, 20% palagonite)

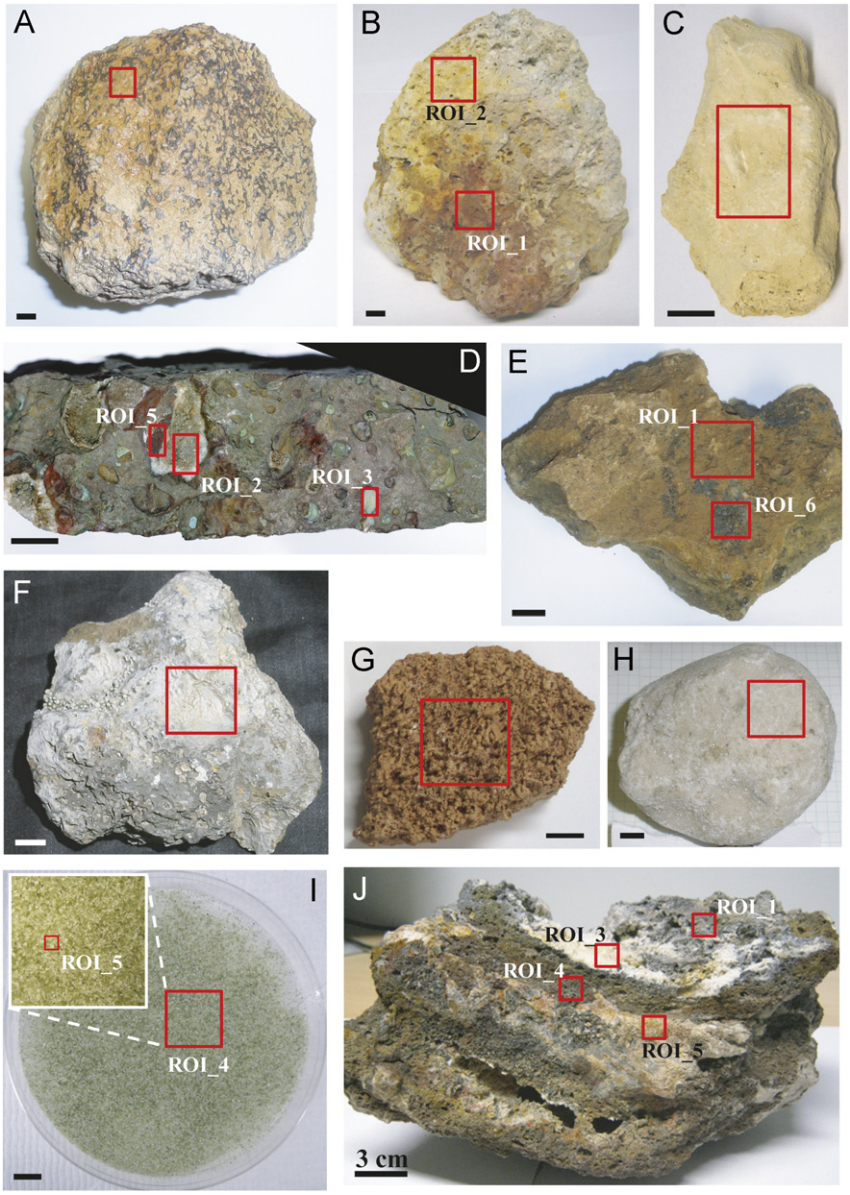

Fig. 3. Mars analogue geological samples used to test the 6 alternative filter sets and bandwidths: (A) NBO; (B) NAL; (C) MAG; (D) SKAFTA; (E) HYALO; (F) KH; (G) GY2; (H) TRONA; (I) XEN; (J) KRAF. Scale bar = 1 cm, unless otherwise stated. Region of Interest (ROI) footprints are indicated in red. (For interpretation of the references to color in this figure legend, the reader is reffered to the web version of this article.)

- JB-JLB-364 (iron oxide + silica + sulfate soil simulant)
- CC-JFM-039-B (JSC Mars-1 + 23.1 wt% gypsum)
- BKR1BE133 (50% olivine, 50% basaltic glass)
- ER-TGS-010 (90% augite, 10% opal-a)

2.2.2. Assessing the performance of filter sets

Filters were assessed based on the following 3 criteria:

Criterion 1. Capturing spectral features (absorptions, peaks): Firstly, a simple assessment of identifying positive or negative capturing of spectral features (e.g., absorptions, reflectance maxima) was conducted on both the database mineral reflectance data, and the Mars analogue sample data. The filter set with the least number of 'spectral misses' is then deemed the best optimised.

Criterion 2. Error score: calculated using Eq. (1) as outlined in Section 2.1. This directly represents how well the filter set reproduces a sample spectrum-the lower the error, the better a filter set captures the sample spectral morphology.

Criterion 3. Discrimination between lithological groups using spectral parameters: different band depths and band slopes were used to classify and group the rock sample ROIs and database minerals based on their spectral morphologies, on the basis that samples/minerals with a similar geochemistry (e.g., iron oxide rich) will cluster into the same group. The parameters used vary slightly between the different filter sets depending on which specific filter wavelengths cover a particular spectral feature, and are detailed in Table 4. These subtle differences can produce notably different results when grouping samples together, which on the Martian surface will be of unknown geochemistry and composition. Five spectral parameter measurements were used: 440–700 nm slope, 950–1000 nm slope, 600 nm band depth, 900 nm band depth, and 950 nm band depth. *K*-means cluster analysis was carried out in Matlab using these five parameters, to identify how the six filter sets group samples of known mineralogy.

The results of these three criteria combined were used to identify which of the six filter sets performed best. This filter set

was then modified further through optimisation of the bandwidths for each of the 12 individual filters within that filter set.

2.3. Multispectral imaging of Mars analogue rocks

Multispectral imaging of the rock samples was conducted using the same set up as described in Cousins et al. (2010), using a 1392 × 1040 Foculus FO432SB camera (CCD detection 400–1000 nm) interfaced with one of two CRI liquid crystal tunable filters (LCTF)-one covering 440–720 nm, the other 650–1010 nm. Imaging of the samples was carried out at a distance of 1.5 m along a horizontal plane. Samples were illuminated with a Solex solar lamp, and a Spectralon reflectance standard was placed in the background of each image for calibration. Multispectral images were processed as described in Cousins et al. (2010) using Image J. Spectra of the ROIs represent the mean of all the pixels within the ROI.

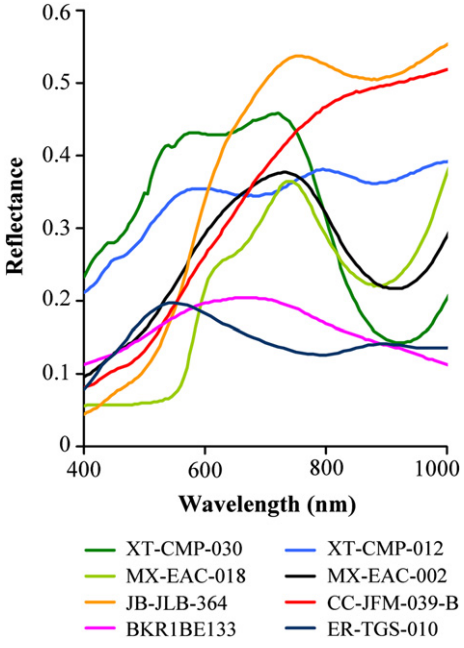

Fig. 4. Mars analogue 'soil' particulate mixtures spectra from the RELAB spectral database.

2.4. Filter bandwidth determination

Once a filter set had been chosen, bandwidths for each of the 12 individual filter wavelengths were determined. The method used is based closely on the method used to determine the optimum centre wavelengths, and the same mineral reflectance input data sets were used. Calculations and optimisation were carried out in Mathcad 8. Several factors have to be considered when optimising bandwidths, and these are detailed below.

2.4.1. Filter transmission

The multispectral filters will be thin film interference filters, and the exact transmission profile of the flight filters will not be known until they are manufactured. However, previous measurements made on the Beagle 2 flight spare and other interference filters have indicated that their transmission profile can be simulated as a Gaussian distribution with reasonable accuracy, and so a Gaussian function was used to simulate the bandwidths. The bandwidth of filters is given as the Full Width at Half Maximum

Table 4
Spectral parameters used to assess the different filter sets (adapted from Farrand et al., 2008). All data are in nm; '*R*' denotes reflectance.

Parameter	Filter set	Representative filter centre wavelengths	Description
440–700 slope	PHYL	440–680	$(R_{680}-R_{440})/(680-440)$
	SULF	440–700	$(R_{700}-R_{440})/(700-440)$
	MAFIC	440–690	$(R_{690}-R_{440})/(690-440)$
	FERRIC	440–670	$(R_{670}-R_{440})/(670-440)$
	ALL_Fe	440–700	$(R_{700}-R_{440})/(700-440)$
	HYDRA	440–710	$(R_{710}-R_{440})/(710-440)$
950–1000 slope	PHYL	960–1000	$(R_{1000}-R_{960})/(1000-960)$
	SULF	950–1000	$(R_{1000}-R_{950})/(1000-950)$
	MAFIC	950–1000	$(R_{1000}-R_{950})/(1000-950)$
	FERRIC	950–1000	$(R_{1000}-R_{950})/(1000-950)$
	ALL_Fe	950–1000	$(R_{1000}-R_{950})/(1000-950)$
	HYDRA	940–1000	$(R_{1000}-R_{940})/(1000-940)$
900 band depth	PHYL	900	$1-(R_{900}/[(0.400*R_{810})+(0.600*R_{960})])$
	SULF	890	$1-(R_{890}/[(0.462*R_{820})+(0.538*R_{950})])$
	MAFIC	900	$1-(R_{900}/[(0.500*R_{850})+(0.500*R_{950})])$
	FERRIC	900	$1-(R_{900}/[(0.455*R_{840})+(0.545*R_{950})])$
	ALL_Fe	890	$1-(R_{890}/[(0.545*R_{840})+(0.455*R_{950})])$
	HYDRA	890	$1-(R_{890}/[(0.385*R_{810})+(0.615*R_{940})])$
600 band depth	PHYL	590	$1-(R_{590}/[(0.667*R_{560})+(0.333*R_{650})])$
	SULF	610	$1-(R_{610}/[(0.500*R_{560})+(0.500*R_{660})])$
	MAFIC	560	$1-(R_{560}/[(0.385*R_{520})+(0.615*R_{640})])$
	FERRIC	610	$1-(R_{610}/[(0.600*R_{570})+(0.400*R_{670})])$
	ALL_Fe	570	$1-(R_{570}/[(0.615*R_{520})+(0.385*R_{650})])$
	HYDRA	590	$1-(R_{590}/[(0.500*R_{550})+(0.500*R_{630})])$
950 band depth	PHYL	960	$1-(R_{960}/[(0.400*R_{900})+(0.600*R_{1000})])$
	SULF	950	$1-(R_{950}/[(0.455*R_{890})+(0.545*R_{1000})])$
	MAFIC	950	$1-(R_{950}/[(0.500*R_{900})+(0.500*R_{1000})])$
	FERRIC	950	$1-(R_{950}/[(0.500*R_{900})+(0.500*R_{1000})])$
	ALL_Fe	950	$1-(R_{950}/[(0.455*R_{890})+(0.545*R_{1000})])$
	HYDRA	940	$1-(R_{940}/[(0.375*R_{890})+(0.625*R_{970})])$

(FWHM) of the transmission curve:

$$T_F(\lambda) = \frac{2.35}{\sqrt{2 \times \pi} \times FWHM_F} \times e^{-(5.52 \times \cdot (\lambda - F)^2 / 2 \times FWHM_F^2)} \quad (3)$$

where T_F is the transmission of the filter at wavelength F, λ is the wavelength, and $FWHM_F$ is the FWHM of the filter at wavelength F.

2.4.2. Determining the effects of bandwidth on error score

The reflectance spectra for the 160 database mineral samples were interpolated at 1 nm intervals over the range 370–1100 nm for the optimisation. The extended wavelength range is required as the tail of the Gaussian profile extends some distance either side of the centre. In some cases the reflectance data did not extend far enough into the UV and so additional data was extrapolated. A set of transmission values were calculated for each of the 12 filters at 1 nm intervals over the range 370–1100 nm. For each filter, the transmission at each wavelength interval was multiplied by a mineral reflectance at each wavelength interval and the resulting dataset was summed to obtain a simulated reflectivity measurement for that filter. This was repeated for each filter (F) and mineral reflectance spectrum (m) in the dataset to obtain simulated reflectance values ($R_{F,m}$) for all filter wavelengths and all minerals:

$$R_{F,m} = \sum_{\lambda=370}^{1100} R_m(\lambda) \times T_F(\lambda) \quad (4)$$

where $R_m(\lambda)$ is the reflectance of mineral m at wavelength λ and $T_F(\lambda)$ is the transmission of filter F at wavelength λ.

As with the filter wavelength optimisation, intermediate data points were calculated using linear interpolation and an error score for each mineral reflectance spectrum was calculated using Eq. (1) (with $N=561$ for 1 nm intervals). An average reflectance spectrum for the filter set over all mineral reflectance spectra in the dataset was then calculated as before using Eq. (2).

2.4.3. Exposure times

The main aim of this work was to develop a filter set with the optimal science output i.e., one which most accurately reproduces the reflectance of the scene. However the filter bandwidth also has significant engineering implications as it affects the sensitivity of the camera system. Although narrow band filters may most accurately reproduce the original spectrum as they do not average out spectral features to the same extent as wide band filters, their low light throughput may have detrimental effects on the captured image which could directly affect the science output. In order to assess the effects the bandwidths may have on the camera sensitivity, typical exposure times for the camera system on the Martian surface were estimated.

Typical exposure times for the wide angle cameras were determined from NASA PDS data from the MER Spirit Pancam instrument, with compensations made for the difference in lens aperture, camera quantum efficiency, filter wavelengths, bandwidths and maximum transmission. Images of the calibration target taken during the first 30 Sols (before the calibration target was contaminated significantly with dust), taken with the full set of filters were analysed. Average exposure values for the 60% reflectance region of the calibration target along with the exposure time were determined for each image. A camera independent exposure factor (I_0)-a factor dependent only on the incident solar illumination and atmospheric absorption—was then calculated from:

$$I_0(\lambda) = \frac{I(\lambda) \times F^2}{t \times R(\lambda) \times T(\lambda) \times BW(\lambda) \times QE(\lambda)} \quad (5)$$

where $I(\lambda)$ is the exposure achieved (as a fraction of the maximum dynamic range) for the region of interest of the image with the filter at wavelength λ, F is the lens F number (f/20 for MER cameras), t is the exposure time of the image taken with the filter at wavelength λ, $R(\lambda)$ is the reflectance of the region of interest (ROI) at wavelength λ (60% throughout the spectrum), $T(\lambda)$ is the maximum transmission of the filter at wavelength λ (assumed to be 90% for all filters), $BW(\lambda)$ is the bandwidth of the filter at wavelength λ and $QE(\lambda)$ is the Quantum Efficiency of the MER PanCam CCD at wavelength λ (from Bell et al., 2003).

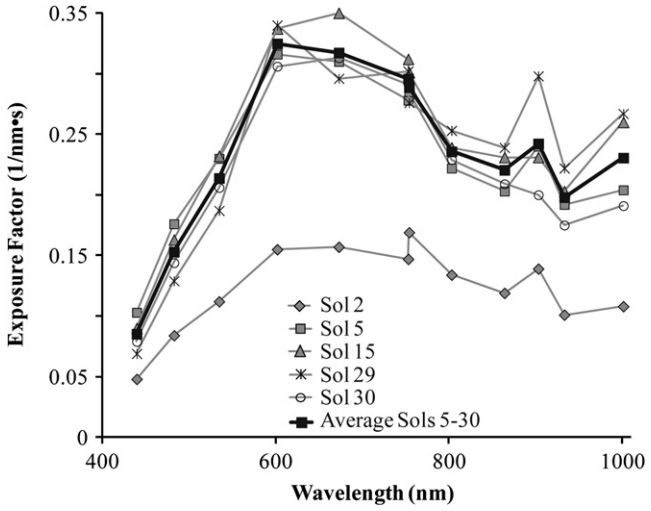

Fig. 5. Camera independent exposure factor calculated from NASA PDS data for the Spirit rover over 5 sols. The average is for the data from sols 5 to 30.

Images from 5 sols were processed and the resultant exposure factors are plotted in Fig. 5. It is apparent from the graph that four of the five datasets match closely whilst the data from sol 2 gives values of approximately half those of the other data. Images from sols 5 to 30 were taken between 10:30 and 13:30 h local true solar time, whilst the sun was near zenith, whilst images from sol 2 were taken around 15:50 with the sun lower in the sky. An average was calculated from the data from sols 5 to 30 which is also shown in Fig. 5.

This averaged exposure factor for sols 5 to 30 was interpolated to the proposed ExoMars PanCam wavelengths and used to calculate exposure times from:

$$t = \frac{F^2}{I_0(\lambda) \times T(\lambda) \times BW(\lambda) \times QE(\lambda)} \quad (6)$$

where $I_0(\lambda)$ is the average exposure factor calculated above, F is the F number (f/10 for ExoMars PanCam WACs), $T(\lambda)$ is the maximum transmission of the filter at wavelength λ (assumed to be 85% based on measurements from Beagle 2 filters), $QE(\lambda)$ is the Quantum Efficiency of the Star 1000 sensor at wavelength λ (calculated from data in the Star 1000 datasheet; Uwaerts, 2006) and other variables are as above. The achieved exposure level $I(\lambda)$ from Eq. (5) is substituted for the target exposure level for the ROI. It was assumed that the target exposure level (as a fraction of its maximum range) would be equal to the reflectance of the ROI in order to make used of the full dynamic range of the camera. In this way a target exposure of 50% would be expected for an ROI with a reflectance of 50%, and so these parameters cancel out.

3. Results and discussion

3.1. Filter wavelengths

Table 5 gives the centre wavelengths generated for the six alternative filter sets by the method outlined in Section 2.1. There are a few similarities between these sets, such as the placement of filters at both 950 nm and around 900 nm, and the generally

equal distribution of filters between the visible and NIR (i.e., there is no concentration of multiple filters to any particular region, for any of the filter sets). All filter sets have 7 filters within the visible (<750 nm), with the exception of filter set "HYDRA" which has 6 filters in this region. This suggests that whilst mineral reflectance spectra in general has most diagnostic absorption bands >1 μm, in the specific case of 440–1000 nm multispectral imaging, the visible spectrum is necessary for the Vis–NIR spectral distinction of different mineral targets. It is noted that whilst the filter wavelengths were selected to a resolution of 10 nm, manufacturing requirements may lead filters to have a centre wavelength within a few nanometers of their specified wavelength, and that the actual wavelength will vary by a few nanometers over the Martian temperature range (Smith et al., 1997a, b).

Table 5
Alternative filter set centre wavelengths (nm) for the 6 new filter sets.

PHYL	SULF	FERRIC	MAFIC	ALL Fe	HYDRA
440	440	440	440	440	440
510	470	500	470	490	500
560	500	530	520	520	550
590	560	570	560	570	590
650	610	610	640	650	630
680	660	670	690	700	710
730	700	740	740	740	760
770	730	780	800	780	810
810	820	840	850	840	890
900	890	900	900	890	940
960	950	950	950	950	970
1000	1000	1000	1000	1000	1000

3.2. Testing on mineral spectral datasets

Filter sets were cross-tested on all the mineral spectra in the dataset (Table 3) to see if, for example, the phyllosilicate-optimised (PHYL) filter set could detect iron oxides, and so forth. Fig. 6 shows the minerals with spectral features that are missed

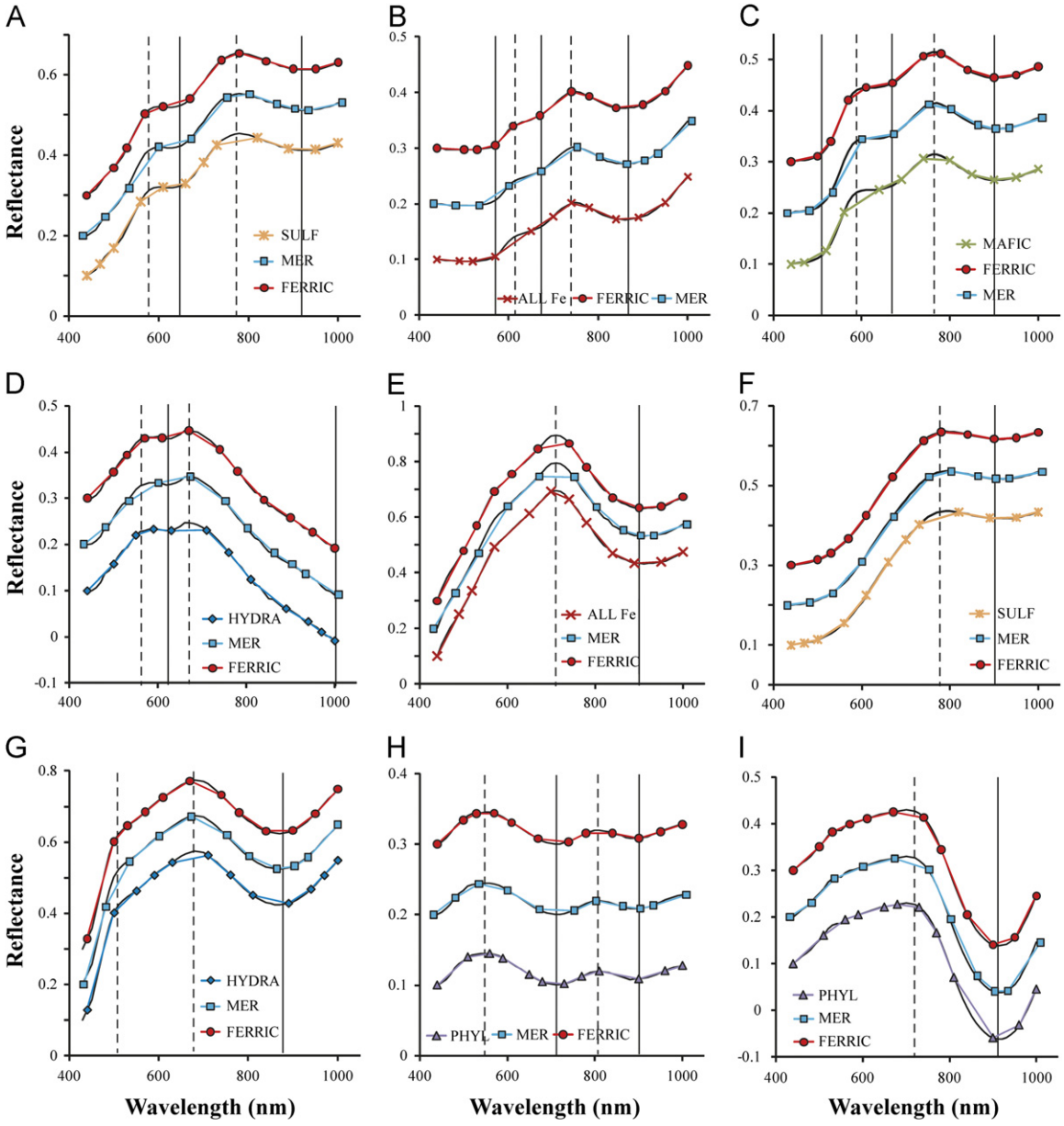

Fig. 6. Minerals with missed spectral features using the 6 alternative filter sets. (A) Nontronite; (B) Haematite; (C) Goethite; (D) Olivine; (E) Jarosite; (F) Ferrihydrite; (G) Copiapite; (H) Chlorite and (I) Orthopyroxene.

by each of the six different filter sets. All positive/negative detections for these filter sets, and also those for past filter sets (MER PanCam and Beagle 2 PanCam), are summarised in Table 6. Filter set FERRIC performs best as its filter wavelengths capture all key absorption and reflectance features of all minerals except the sulfate mineral jarosite, where the filters miss the very top part of the reflectance maximum at ~720 nm. Likewise, filter set F2-12 previously devised by Cousins et al. (2010) also performs well, only missing spectral features in two minerals (haematite and olivine). HYDRA has the most negative detections, failing to capture key features of 6 minerals, most likely due to the bias of the filters towards the 900–1000 nm region. For comparison, the Beagle 2 and MER Pancam filter wavelengths (and therefore by association those for the IMP) perform worst with this dataset, missing spectral features from copiapite, jarosite, nontronite, chlorite, haematite, goethite, olivine, orthopyroxene, and siderite.

3.3. Testing on Mars analogue rocks and soil mixtures

3.3.1. Sample mineralogy

Raman spectroscopy and XRD were used to identify surface and bulk mineralogy of the rock sample ROIs, respectively. As expected for natural samples, most ROIs were found to be heterogeneous, comprising of several mineral components. Fig. 7 shows the Raman spectra for samples NBO, NAL, SKAFTA, KRAF, MAG, TRONA, and XEN, and Table 7 summarises the mineral species identified from both Raman and/or XRD analysis. Collectively, sample ROIs contain: jarosite (sulphate); clinoptilolite, heulandite, analcime, and philipsite (zeolites); haematite (iron oxide); magnesite, calcite, and trona (carbonates); opaline silica; smectite/palagonite; and forsterite, anorthite, albite, and enstatite. Samples HYALO and HH are comprised almost entirely of palagonite, and as such are an undefined mixture of poorly crystallised/microcrystalline smectite clays, nano-crystalline ferric oxides, and zeolites (Bishop et al., 2002; Stroncik and Schmincke, 2002).

3.3.2. Sample ROI reflectance spectra

Sample ROIs used for testing the filter sets are shown in Fig. 3. ROIs were chosen based on visible colour and structural differences observed on the rock surface. Fig. 8 shows the ROI spectra obtained from the multispectral images, along with measured Vis–NIR spectra of both spot points within the ROI's, and/or powdered (<500 μm) ROI samples where possible. Even within the limited spectral range of PanCam (440–1000 nm), there are a variety of spectral morphologies observed in these rocks, and generally sample ROI reflectance profiles are consistent with their mineralogy. Samples NBO and NAL are rich in the iron sulfate jarosite, and as such display a strong absorbance at ~900 nm, typical of Fe^{3+}, as well as smaller absorptions at ~670 and ~500 nm. NAL ROI_1 also has an absorption at ~550 nm, due to the additional presence of haematite. Similarly SKAFTA ROI_5 is consistent with its haematite composition.

Samples HYALO and HH are both Icelandic hyaloclastites/hyalotuffs comprising almost entirely of palagonite. Palagonite is a generic term used to describe the poorly-crystalline alteration products of basalt glass (sideromelane), and is common amongst volcanic regions such as Iceland and Hawaii. It is thought to be similar to the altered basaltic fines on Mars (Bishop et al., 2002), and is commonly used as a Vis–NIR spectral analogue for Martian dust. Specifically, nanophase ferric oxides are an important component of palagonite, particularly those that exhibit a red slope in their reflectance profile. Both samples exhibit a steep ferric absorption edge (Fig. 8), and their spectra also contain a noticeable absorption at ~680 nm, most likely due to small quantities of crystalline iron oxides or smectites (not detected by XRD or Raman). Fe/Mg smectites are the most common alteration mineral on Mars, especially throughout Noachian

Table 6
Positive (+) or negative (−) representation of database mineral spectra. Features missed are given in italics-wavelengths for absorption features (*abs.*), shoulders (*sh.*), and maxima (max.) are in nm.

Target	Mineral	PHYL	SULF	MAFIC	FERRIC	HYDRA	ALLFe	B2	F2-12
Sulfate	Alunite	+	+	+	+	+	+	+	+
	Gypsum	+	+	+	+	+	+	+	+
	Copiapite	+	+	+	+	−(680 max.)	+	−(510 *sh.* & 680 max.)	+
	Jarosite	+	+	+	-(710 max.)	+	+	-(580 *sh.* & 710 max.)	+
	Mg sulfate	+	+	+	+	+	+	+	+
Phyllosilicate	Nontronite	+	−(580 *sh.* & 780 max.)	−(580 *sh.*)	+	−(650 *abs.*)	+	−(580 *sh.* & 650 *abs.*)	+
	Chlorite	+	+	+	+	+	+	−(560 max. & 700 *abs.*)	+
	Montmorillonite	+	+	+	+	+	+	+	+
	Saponite	+	+	+	+	−	+	+	+
Iron oxide	Haematite	−(610 *sh.*, 850 *abs.*)	−(750 max.)	−(610 *sh.*.)	+	−(610 *sh.*, 670 *abs.*, 850 *abs.*)	−(610 *sh.*)	−(560 *abs.*)	−(610 *sh.*)
	Ferrihydrite	+	−(780 max.)	+	+	+	+	+	+
	Magnetite	+	+	+	+	+	+	+	+
	Goethite	+	−(510 *abs.*, 580 *sh.*., 760 max.)	−(580 *sh.*, 760 max.)	+	−(510 & 650 *abs.*)	−(580 *sh.*)	−(580 *sh.*)	+
Mafic silicate	Olivine	−(620 *abs.*)	+	+	+	−(670 max.)	−(620 *abs.*, 670 max.)	−(570 *sh.*, 620 *abs.*)	−(620 *abs.*, 670 max.)
	CPX	+	+	+	+	+	+	+	+
	OPX	+	+	+	+	+	+	−(700 max.)	+
	Albite	+	+	+	+	+	+	+	+
Carbonate	Calcite	+	+	+	+	+	+	+	+
	Magnesite	+	+	+	+	+	+	+	+
	Siderite	+	+	+	+	+	+	−(700 max.)	+
Other	Opal-a	+	+	+	+	+	+	+	+

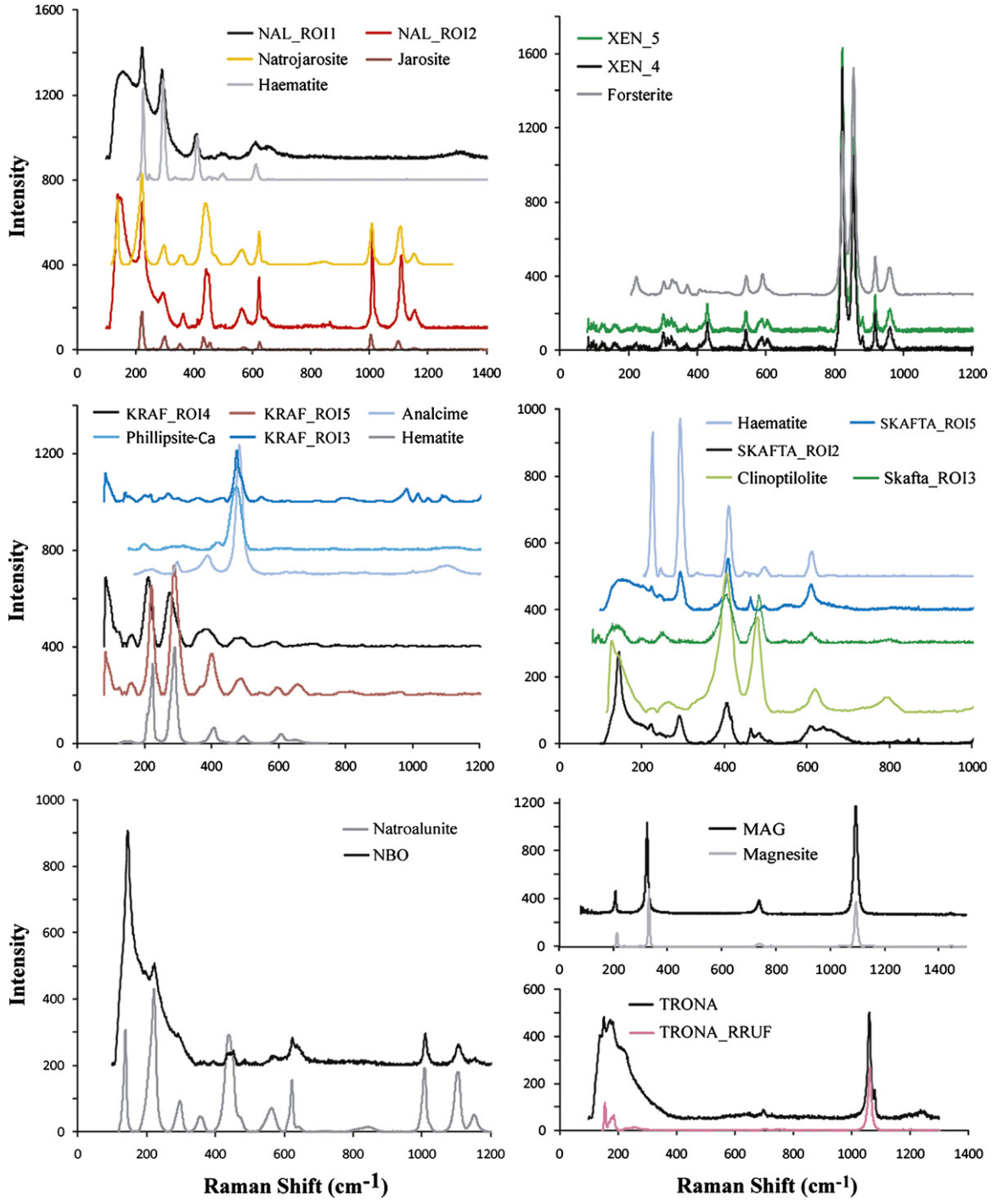

Fig. 7. Raman spectra of selected Mars analogue rock sample ROIs. Reference mineral spectra are also shown (available from the RRUFF online database).

terrains (Ehlmann et al., 2009), and as such are likely targets to be encountered by the ExoMars rover.

There were a variety of zeolites present within these samples, typical for low-temperature hydrothermal alteration of basalts (Warner and Farmer, 2010). Target SKAFTA ROI_3 contains heulandite and clinoptilolite (see Fig. 7 and Table 7) as vesicle deposits within a basaltic lava, and the spectrum of this target is consistent with that of heulandite with an absorption at ~720 nm. Target KRAF ROI_3 consists of analcime and phillipsite (Fig. 7), and its broad spectral shape is again consistent with this, save for the possible Fe-absorption at 680 nm (Fig. 8). Similarly, carbonate samples typically have featureless spectral profiles in the PanCam spectral range, and samples MAG and TRONA are consistent with this. TRONA displays a slight absorption at 1000 nm, likely echoing water absorptions further into the infrared. Samples GY2 and KH also exhibit featureless spectra, again consistent with opaline silica. This absence of spectral features mean rock targets such as these could not be distinguished from each other with PanCam multispectral data alone, regardless of the filter wavelengths chosen. Given the importance of these minerals and lithologies as astrobiological targets (i.e., indicative of a potentially habitable palaeoenvironment), more work should be conducted to explore the remote identification/discrimination of these targets with multispectral data.

Table 7
Mineral species present in Mars analogue rock samples as identified with either Raman and/or XRD.

Sample	ROI	Mineralogy
GY2	ROI_1	Opaline silica, calcite
HH	ROI_1	Smectite, Montmorillonite (?)
HYALO	ROI_1	*Amorphous*
	ROI_4	Anorthite, Augite[a]
	ROI_5	Albite, Forsterite[a]
	ROI_6	Labradorite, Diopside/ Augite[a]
KH	ROI_1	Opaline silica, calcite
KRAF	ROI_1	Haematite
	ROI_3	Analcime, Ca-phillipsite, Sulfur
	ROI_4	Haematite
	ROI_5	Hematite, Anorthite, Augite/ Diopside
MAG	ROI_1	Magnesite, dolomite
NAL	ROI_1	Haematite
	ROI_2	Natrojarosite
NBO	ROI_1	Natrojarosite
SKAFTA	ROI_2	Quartz, Hematite, Heulandite, Clinoptilolite
	ROI_3	Clinoptilolite, Heulandite
	ROI_5	Haematite
TRONA	ROI_1	Trona
XEN	ROI_4	Forsterite, Enstatite
	ROI_5	Forsterite

[a] Residual, unaltered basaltic component amongst the largely amorphous palagonite matrix.

Finally, peridotite sample XEN shows characteristic absorption features indicative of both olivine (630 nm absorption) and orthopyroxene (900 nm absorption). XRD data indicates these components are forsterite (Mg-rich olivine) and enstatite (Mg-rich pyroxene), respectively. Whilst not necessarily astrobiological targets in their own right, the identification of olivine especially can be used to deduce the level of aqueous alteration (Hausrath et al., 2008a, b), thus providing constraints on the presence of liquid water within the area.

3.3.3. Filter set sub-sampling of rock ROIs and soil spectra

The rock sample ROI multispectral data and RELAB soil spectra were sub-sampled to match the centre wavelengths of the 6 different filter sets (examples shown in Fig. 9). As with the mineral dataset, filters were assessed in their positive/negative capturing of spectral features, such as absorption bands and reflectance maxima. These results are given in Table 8, and again show filter set FERRIC to perform best out of all the filter sets. Three out of four sample spectra that were not captured by the FERRIC filter set were RELAB soil spectrum XT-CMP-030 (25% olivine+75% bronzite), and rock samples XEN ROI_4 and ROI_5. This is due to the filters missing the small, but well defined, 630 nm olivine absorption, which falls between filters at 610 and 670 nm. Filter set PHYL also performs well, but misses spectral features of a wider range of lithological targets, including those that contain zeolites, haematite, smectite, and pyroxene-all minerals common to Mars (except perhaps zeolite) and also with strong spectral features in the PanCam range. Filter set SULF commonly misses absorptions in iron-bearing minerals and targets, such as those containing haematite (Fig. 9A), jarosite, olivine, pyroxene, and palagonite. This is also largely true of the original Beagle 2 filter wavelengths, and also filter sets HYDRA and ALLFe. The inability of ALLFe to capture spectral features within iron-bearing minerals and rock ROIs is unexpected, given that the input data to calculate this filter set consisted of minerals with Fe absorptions. However, this filter set also had the largest input dataset (13 mineral species), and this could have led to the filter set being too generic.

Astrobiologically interesting but featureless spectra such as carbonates and opaline silica are reproduced by all filter sets. As such, whilst this lack of spectral features mean discrimination between them using PanCam data is unlikely, the lithologies dominated by these minerals will be equally well-represented regardless of the filter set chosen. Conversely the spectrum of zeolite mineral heulandite (which has relatively well-defined spectral features) within rock target SKAFTA ROI_3 is missed by filter sets PHYL, SULF, and HYDRA. These three filter sets all miss the reflectance maximum at 840 nm, due to a gap of 70–90 nm (depending on filter set) between filters 800/810 nm and 890/900 nm (Fig. 9B).

3.3.4. Error scores

The absolute measured differences between filter-generated spectra and the original rock ROI or soil spectra were calculated. Table 9 summarises these results, showing those filters with both the lowest error scores (i.e., the best filter set), and also the second lowest error scores to account for the fact that often there is little difference between these two. Filter set FERRIC has either the lowest or second lowest error for 24 out of 32 rock ROI and soil targets. Fig. 10 shows both the total error score from all targets for each filter set (Fig. 10A), as well as the frequency of lowest error score (Fig. 10B). There is little difference between PHYL, SULF, MAFIC, ALLFe, and HYDRA filter sets in their total error score, with FERRIC being noticeably lower by comparison. Likewise, FERRIC has the highest frequency of the lowest calculated error score across the rock ROI/soil targets.

3.4. Sample discrimination

Spectral parameters such as band depth and slope can be used to group PanCam targets based on their spectral properties (e.g., Farrand et al. 2006; 2007). In particular, such parameters can sometimes be linked to particular geochemical qualities, such as the presence of iron (900 nm band depth), level of oxidation (440–700 nm slope) and hydration (950–1000 nm slope, Rice et al. 2010). The selection of filter centre wavelengths will affect how PanCam targets are represented by these spectral parameters, and ultimately their interpretation. Fig. 11 shows 950–1000 nm slope plotted against 900 nm band depth for all six filter sets. These two parameters should correlate to each other, in that if a spectrum has a band centred at 900 nm, it will have a lower absorption at 1000 nm (i.e., forming a slope between 950 and 1000 nm). Fig. 11 shows the correlation between these two parameters. Additionally, samples plot within quadrants specific to their broad geochemical composition. The top right quadrant (grey in Fig. 11) is characterised by an absorption at 900 nm coupled with no absorption at 1000 nm. As such, this space is populated by the iron-rich sulfates (jarosite, copiapite), ferric oxides (haematite, goethite, ferrihydriate) and iron-rich phyllosilicates (nontronite). Conversely, the lower left quadrant is characterised by absorption at 1000 nm combined with no absorption at 900 nm. As such, this space is populated by pale coloured carbonates and sulfates with hydration features. This region (highlighted in blue in these plots, Fig. 11) could tentatively be used to identify astrobiological targets amongst outcrops imaged on Mars by PanCam. In the case of this sample set, this would include the carbonates magnesite and trona, sulfates gypsum and magnesium sulfate, and (depending on the filter set) silica sinter sample GY2. Likewise, the grey region in these plots can be used to identify those targets that are iron rich. However, the lack of hydration features until further into the infrared means there is no way of telling with PanCam data alone if these minerals are hydrated (e.g., jarosite) or not (e.g., haematite).

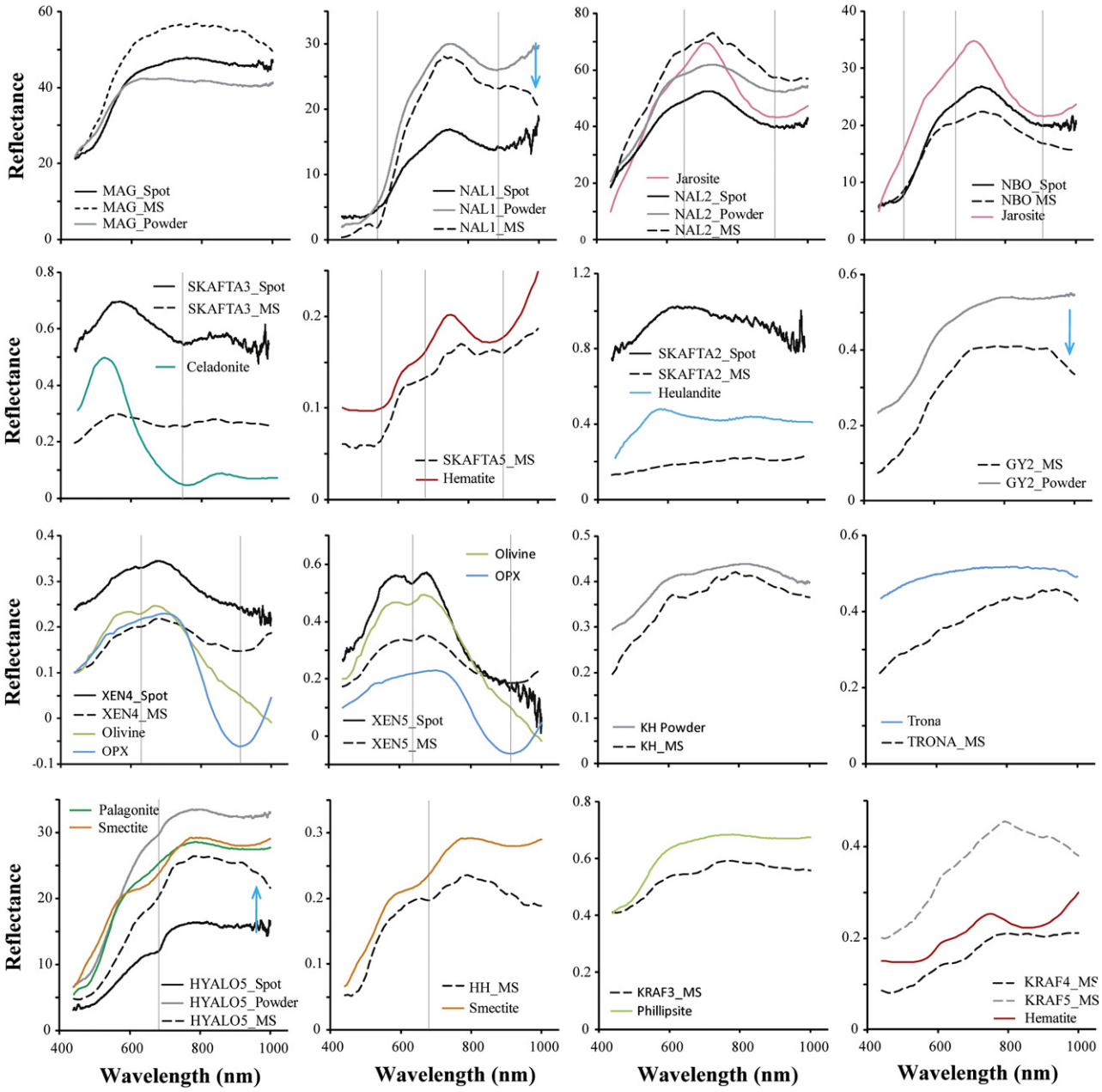

Fig. 8. Rock sample ROI multispectral ("MS"), surface, & powdered Vis–NIR spectra, together with selected database mineral spectra for comparison. Blue arrows highlight an IR absorption that is only seen in the multispectral data, and not the reflectance spectral data (powdered or spot target), and therefore may be an artefact. Reflectance is given as a % of the calibration target. (For interpretation of the references to color in this figure legend, the reader is reffered to the web version of this article.)

There are several differences in where samples plot between the different filter sets. One notable difference is that filter set PHYL incorrectly plots rock target Skafta_ROI_3 (clinoptilolite and heulandite) as having no 900 nm iron absorption-an issue that is also reflected in the incomplete capturing of the sample spectrum by filter set PHYL (Fig. 9). Additionally, the correlation between these two parameters is greatest using the FERRIC filter set.

Finally, *K*-means cluster analysis was used to group all database mineral spectra and sample ROI multispectral data into three categories based on the sample/mineral chemistry and identifiable spectral signatures (Appendix A). Minerals were categorised as follows:

- Fe-containing minerals and those samples with Fe-absorptions.
- Non-Fe containing hydrated minerals and those samples/minerals with a hydration absorption at 1000 nm.
- All other samples that do not fit into either of the above two groups.

K-means clustering into three groups was conducted to represent these three categories. Input data for the cluster analysis consisted of the values calculated using the six filter sets for the following parameters: 440–700 nm slope, 950–1000 nm slope, 900 nm band depth, 950 nm band depth, and 600 nm band depth. Fig. 12 shows the plots of these groups for the different filter sets. Filter set PHYL exhibits poor differentiation between the non-Fe hydrated mineral/sample spectra and those with strong Fe absorptions. Likewise, filter sets MAFIC and ALL_Fe produce groups that are not represented by any clear spectral morphology, with the exception of the last group that consists of just one sample. SULF, FERRIC, and HYDRA all produce the most effective groupings with a consistent spectral morphology present in all three groups, and with a clear discrimination between

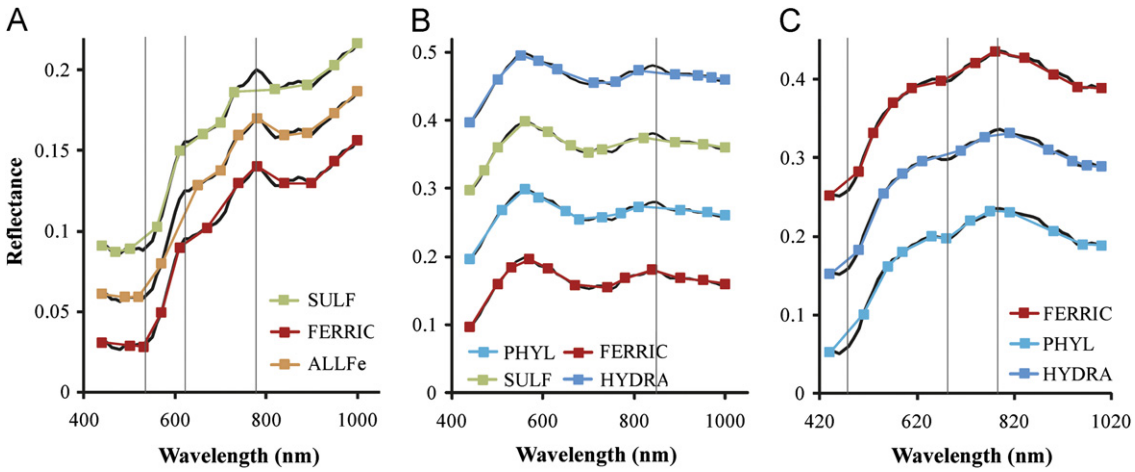

Fig. 9. Examples of three ROI targets within Mars analogue rock samples, showing the missing of spectral features by particular filter sets, and the capturing of spectral features by the FERRIC filter set; (A) haematite target SKAFTA_ROI5; (B) heulandite target SKAFTA_ROI3; (C) smectite target HH. Black spectra are the complete spectrum for each ROI as acquired with multispectral imaging. Grey lines show where spectral features (absorptions, maxima) are missed. NB: spectra are separated for clarity. Reflectance is given as a % of the calibration target.

Table 8
Positive (+) or negative (−) representation of minerals in Mars analogue rock sample ROIs, and RELAB soil mixture spectra.

Target	Broad mineralogy	PHYL	SULF	MAFIC	FERRIC	HYDRA	ALLFe	B2	F2-12
XEN_ROI4	Olivine+pyroxene	+	−	−	−	−	−	−	−
XEN_ROI5	Olivine+pyroxene	+	−	−	−	−	−	−	−
Skafta_ROI2	Quartz	+	+	+	+	+	+	+	+
Skafta_ROI3	Clinoptilolite+heulandite	−	−	+	+	−	+	+	+
Skafta_ROI5	Haematite	−	−	−	+	−	−	−	−
NBO	Jarosite	+	+	−	+	+	−	−	+
NAL_ROI1	Haematite+jarosite	+	+	+	+	+	+	+	+
NAL_ROI2	Jarosite	+	+	−	+	−	−	−	+
MAG	Magnesite	+	+	+	+	+	+	+	+
KH	Opaline silica+calcite	+	+	+	+	+	+	+	+
HH	Palagonite/smectite	−	−	+	−	−	+	−	−
GY2	Opaline silica	+	+	+	+	+	+	+	+
HYALO_ROI1	Palagonite	+	+	−	+	−	−	+	+
HYALO_ROI4	Basalt	+	+	+	+	+	+	+	+
HYALO_ROI5	Palagonite	+	+	−	+	−	−	+	+
HYALO_ROI6	Basalt+palagonite	+	+	+	+	+	+	+	+
KRAF_ROI1	Basalt	+	+	−	+	−	−	+	−
KRAF_ROI3	Analcime+phillipsite	+	−	−	+	−	−	+	+
KRAF_ROI4	Basalt+haematite	+	−	−	+	−	−	+	−
KRAF_ROI5	Basalt+haematite	−	−	−	+	−	−	−	−
Trona	Sodium carbonate	+	+	+	+	+	+	+	+
XT-CMP-030	Olivine+bronzite	+	+	+	−	+	+	−	+
XT-CMP-012	Calcite+chlorite	+	+	+	+	+	+	+	+
MX-EAC-018	Pyroxene+haematite	−	+	+	+	−	−	−	−
MX-EAC-002	Pyroxene+palagonite	+	−	+	+	+	+	+	+
JB-JLB-364	Iron oxide+silica+sulfate	+	−	+	+	+	+	+	+
CC-JFM-039-B	Mars 1+gypsum	+	+	+	+	+	+	+	+
BKR1BE133	Olivine+basalt glass	+	+	+	+	+	+	+	+
ER-TGS-010	Augite+opal a	+	+	+	+	+	+	+	+

non-Fe hydrated minerals/samples and those with strong Fe absorptions. Regardless of filter set, iron oxide mineral magnetite was misclassified and grouped with the hydrated minerals such as carbonates, and non-Fe containing sulfates/phyllosilicates. This is due to the lack of significant Fe-absorptions, and so producing a flat, featureless spectrum. Similarly, nontronite was also commonly grouped with these hydrated minerals, despite the Fe-absorptions in its reflectance. It is groupings such as this that will provide initial division of broad lithological groups based on spectral differences.

3.5. Selection of the FERRIC filter set

Overall, the FERRIC filter set captured the spectral features of more minerals and rock ROI targets than any other filter set. The consistent ability of the FERRIC filter set to out-perform the other filter sets lies firstly in the dominance of iron-bearing mineral species (including both sulphates and phyllosilicates) within the Mars analogue rock targets themselves, but also in the presence of strong $Fe^{2+/3+}$ absorptions within the wavelength range visible to PanCam. Importantly, other non-Fe containing mineral targets within the rock ROIs were effectively captured with the FERRIC filter set (Table 9). For example, rock target KRAF_ROI3 comprises of the zeolite minerals analcime and Ca-bearing phillipsite, and is reproduced with the lowest error by the FERRIC filter set. Likewise, the featureless nature of the carbonate and opaline silica samples mean the FERRIC filter wavelengths (and indeed those of the other five filter sets) could easily capture their spectral morphology.

The FERRIC filter set also provided well defined *K*-means groups, producing a clear division between broad spectral groups. This, combined with its ability to effectively capture mineral and rock ROI spectral features with the lowest degree of error, leads to the recommendation of the centre wavelengths of this filter set as the replacement to the baseline Beagle 2 filter wavelengths for the ExoMars PanCam.

3.6. Bandwidth optimisation of the FERRIC filter set

As with the six alternative filter sets, bandwidths were tested by calculating an error score to determine the accuracy with which the filter set reproduced reflectance spectra. In order to assess the overall effect of the bandwidth on the error score, mean error scores were calculated using 160 database reflectance spectra (all spectra used to develop filter sets PHYL, SULF, FERRIC and MAFIC–see Table 3–and additional carbonate and opal minerals) over a range of uniform bandwidths. For comparison the mean error scores for the same reflectance data and bandwidths were calculated for the MER, Beagle 2 and F2-12 filter sets, and are plotted in Fig. 13. It can be seen that the error score increases with bandwidth as would be expected, but it is also clear that the FERRIC filter set performs better for all bandwidths than either the MER of Beagle 2 filter sets with the same bandwidths. F2-12 performs similarly well. For all filter sets, the minimum error is achieved for bandwidths between 5 and 10 nm. Notably, the FERRIC filter bandwidths could be uniformly increased to 30 nm and still achieve a lower error score than the Beagle 2 filter set at its best. The most likely reason that the MER cameras show a large error score is that the MER Pancam instruments feature only 11 geology filters instead of the 12 used in other previous missions.

Whilst the FERRIC filter wavelengths successfully captured nearly all the rock target ROIs and RELAB soils tested, those targets containing olivine and therefore exhibited an absorption feature at 630 nm, were poorly reproduced. The closest filter to this absorption is the one placed at 610 nm, but this filter has a very narrow optimised bandwidth of 10 nm. Fig. 14 shows how this filter set and respective bandwidths would miss this absorption. Therefore with this filter set, the remote detection of olivine using PanCam multispectral data is potentially compromised, and demonstrates the difficulty in reproducing a range of spectral morphologies when limited to 12 wavelengths.

It is evident from Fig. 13 that bandwidths can be increased within a limited range without having too detrimental an effect on the error score and therefore the accuracy of the measured spectrum. The bandwidths can therefore be used to optimise the exposure times of the cameras. Exposure times for the FERRIC filter set with a 10 nm bandwidth for all filters were calculated as outlined in Section 2.3.3 and are plotted in Fig. 15. It can be seen that at either end of the spectral range where both the QE of the detector and incident solar spectrum are lower, the exposure times are considerably longer than for the centre of the spectrum. In particular the 1000 nm filter may require an exposure time almost 30 times longer than for the 610 nm filter.

The estimated exposure times are likely to be the shortest when the sun is near zenith and when imaging a high reflectance scene. If the camera were set to correctly expose a darker scene (maximum reflectance 50%-typical for many rocks, minerals and soils) then the exposure times could be double those shown. If images are taken later in the day (as for the sol 2 data in Fig. 5) then exposure times could double again. Calculations for the Imager for Mars Pathfinder indicated that light intensity could

Table 9
Filter sets with the lowest calculated error scores. The associated plot (Fig. 10) shows "FERRIC" to have the lowest error scores overall.

Target	Broad mineralogy	Lowest error	Second lowest error
XEN_ROI4	Olivine+pyroxene	SULF	PHYL
XEN_ROI5	Olivine	PHYL	MAFIC
Skafta_ROI2	Quartz	FERRIC	MAFIC
Skafta_ROI3	Clinoptilolite+heulandite	MAFIC	FERRIC
Skafta_ROI5	Haematite	FERRIC	HYDRA
NBO	Jarosite	FERRIC	HYDRA
NAL_ROI1	Alunite+jarosite	HYDRA	SULF
NAL_ROI2	Jarosite	SULF	FERRIC
MAG	Magnesite	SULF	FERRIC
TRONA	Carbonate	HYDRA	SULF
GY2	Opal-a	HYDRA	SULF
KH	Opal-a	SULF	FERRIC
HH	Smectite/palagonite	ALLFe	MAFIC
HYALO_ROI1	Palagonite	FERRIC	SULF
HYALO_ROI4	Basalt	FERRIC	SULF
HYALO_ROI5	Palagonite	FERRIC	SULF
HYALO_ROI6	Basalt+palagonite	All_Fe	SULF
KRAF_ROI1	Basalt	SULF	FERRIC
KRAF_ROI3	Zeolite	FERRIC	SULF
KRAF_ROI4	Basalt+haematite	FERRIC	MAFIC
KRAF_ROI5	Basalt+haematite	FERRIC	MAFIC
XT-CMP-030	Olivine+bronzite	All_Fe	MAFIC
XT-CMP-012	Calcite+chlorite	All_Fe	HYDRA
MX-EAC-018	Pyroxene+haematite	FERRIC	SULF
MX-EAC-002	Pyroxene+palagonite	FERRIC	ALLFe
JB-JLB-364	Iron oxide+silica+sulfate	FERRIC	HYDRA
CC-JFM-039-B	Mars 1+gypsum	All_Fe	MAFIC
BKR1BE133	Olivine+basalt glass	SULF	FERRIC
ER-TGS-010	Augite+opal a	PHYL	FERRIC

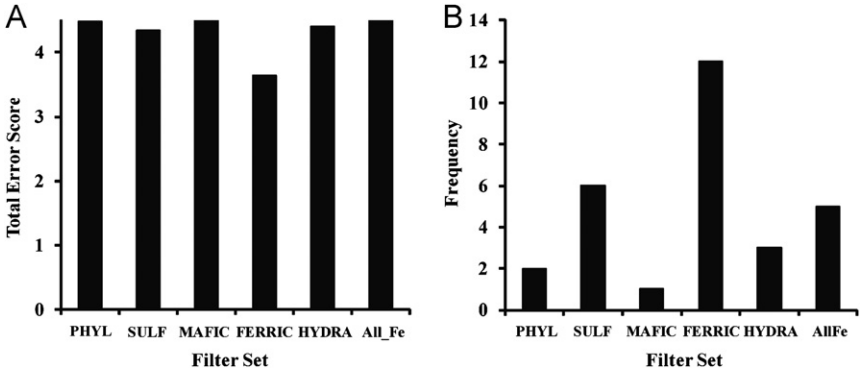

Fig. 10. (A) Total measured error between filter set—generated spectra and complete spectra, for each of the filter sets and (B) frequency of each filter set having the lowest error when tested on all Mars analogue rock ROIs and RELAB soil spectra.

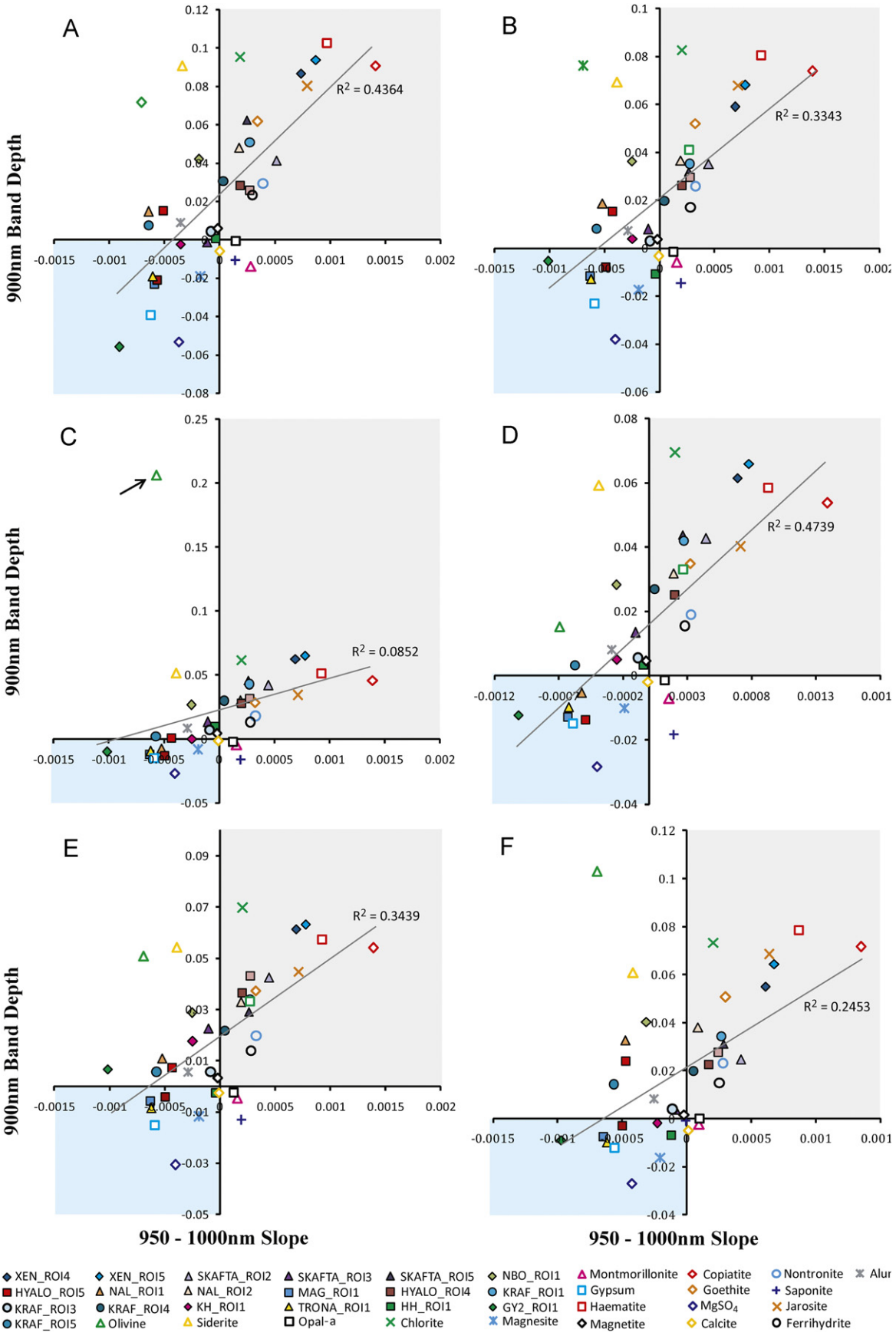

Fig. 11. Spectral parameter plot of 950–1000 nm Slope vs. 900 nm Band Depth, for all Mars analogue rock ROIs and mean mineral spectra (Fig. 2); (A) PHYL; (B) SULF; (C) MAFIC; (D) FERRIC; (E) ALLFe; (F) HYDRA. Blue quadrant represents those minerals with a 'hydrated' signature (negative 950–1000 nm slope), grey quadrant represents those minerals with an Fe-rich composition (900 nm Band Depth). (For interpretation of the references to color in this figure legend, the reader is reffered to the web version of this article.)

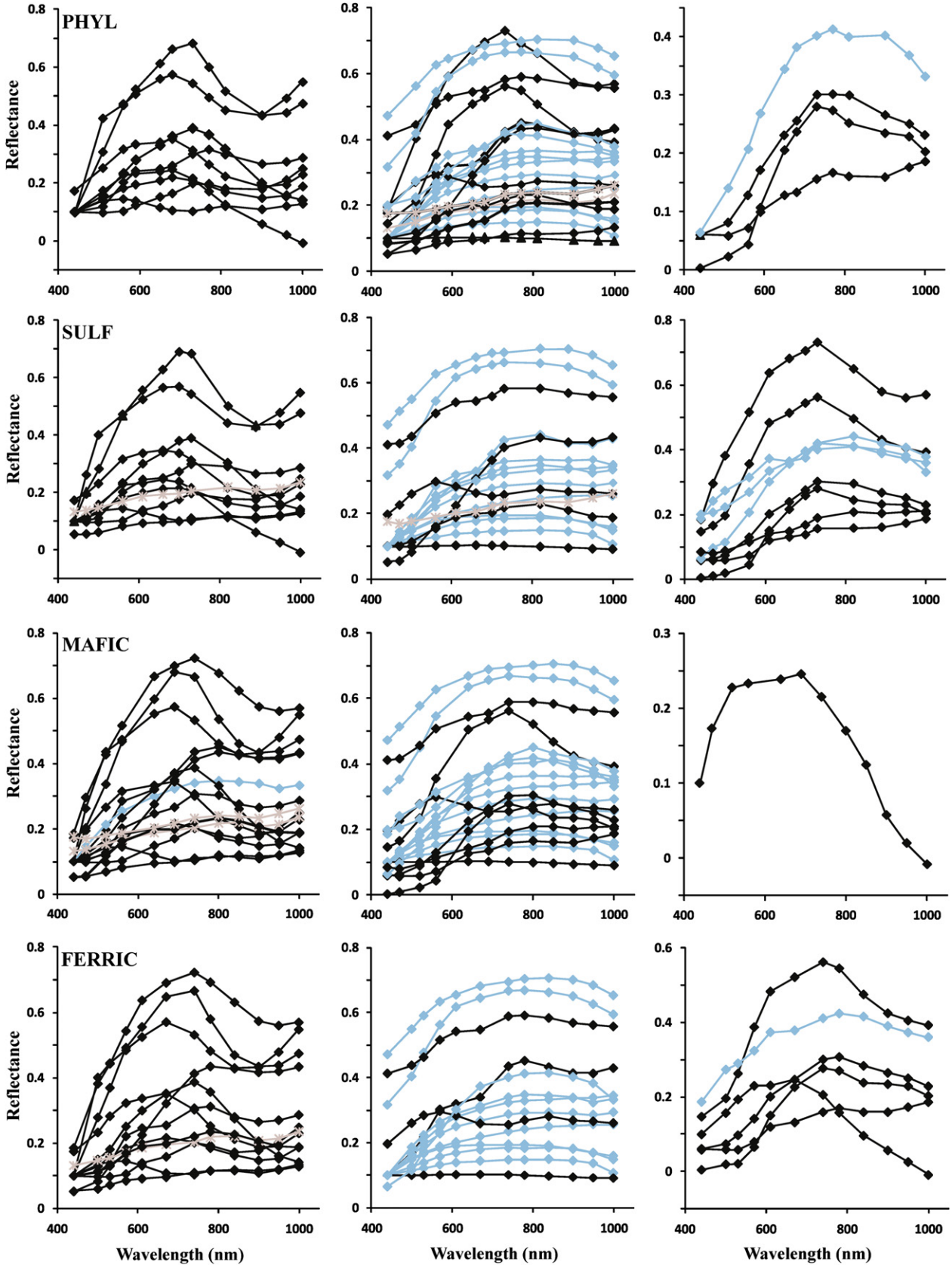

Fig. 12. *K*-means classification for the 6 alternative filter sets, based upon the following spectral parameters: 440–700 nm Slope, 950–1000 nm Slope, 900 nm Band Depth, 950 nm Band Depth, and 600 nm Band Depth; using 100 iterations. Three groups were used to represent: 1- Fe-containing minerals and those with Fe absorptions (black); 2- non-Fe containing hydrated minerals and those with a hydration signature (blue); 3-all other samples which were neither (grey). (For interpretation of the references to color in this figure legend, the reader is referred to the web version of this article.)

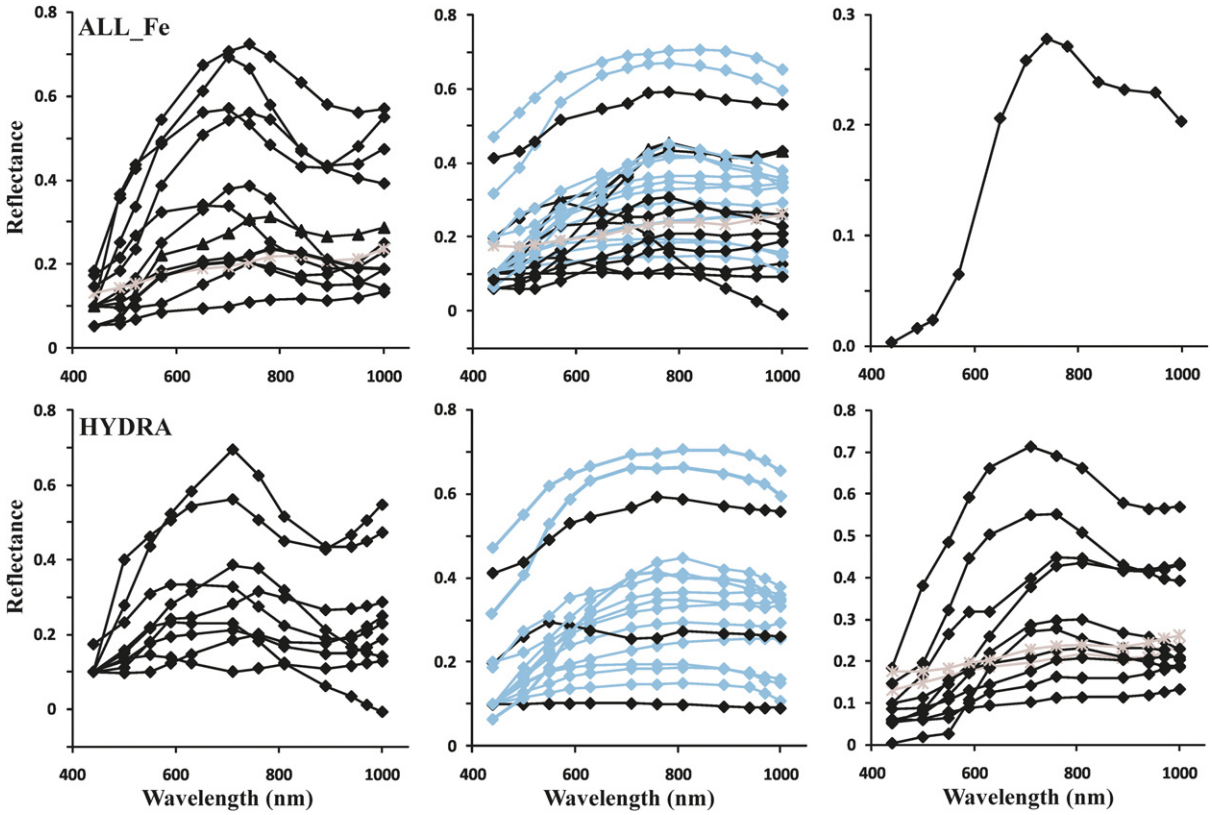

Fig. 12. (*continued*)

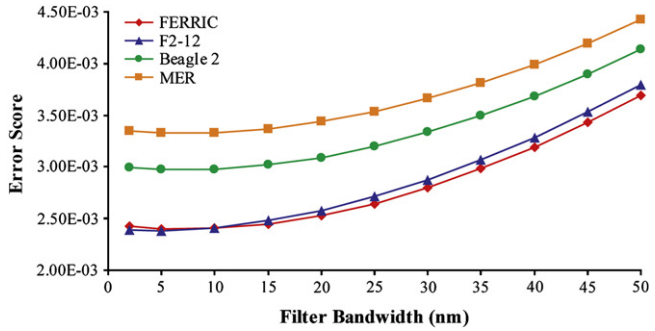

Fig. 13. Plot showing increasing error as the filter bandwidths are increased, for the FERRIC, F2-12, Beagle 2, and MER filter centre wavelengths.

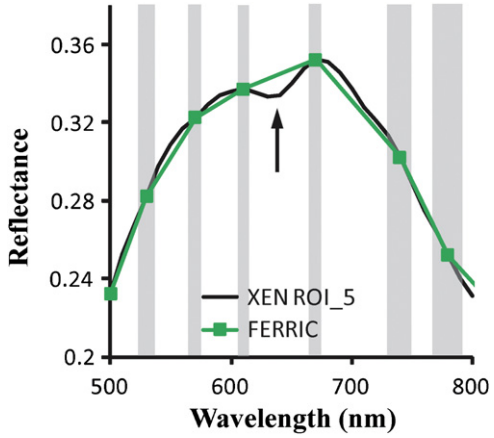

Fig. 14. Close up of the 630 nm spectral feature in olivine-rich rock sample target XEN ROI_5 that is missed with the FERRIC filter set optimised centre wavelengths and bandwidths (grey lines). Reflectance is given as a % of the calibration target.

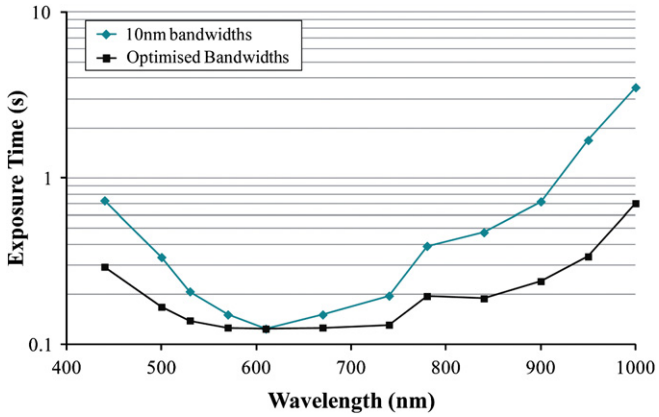

Fig. 15. Calculated exposure times at each filter wavelength for uniform (10 nm) and optimised bandwidths for the FERRIC filter set.

drop by a factor of 30 (Smith et al., 1997a, b) near sunset requiring exposure times approaching 4 min for the 1000 nm filter. This is clearly a very long exposure time and so would likely result in increased image noise. It is therefore believed that it is justifiable to increase the bandwidth of some filters to reduce exposure time at the expense of error score.

Filter bandwidths were determined which provide more uniform exposure times without compromising the effectiveness of the filter set. The exposure times with these optimised bandwidths are shown in Fig. 15. The optimised filter wavelengths and bandwidths are presented in Table 10 and the modelled filter transmission profiles are shown in Fig. 16. When compared to the filter sets from previous missions, the proposed filters generally have narrower bandwidths in the visible spectrum and wider in the NIR. The increased bandwidth in the NIR is attributable to the

Table 10
Filter characteristics for the FERRIC filter set for the ExoMars Panoramic Camera.

Filter number	Centre wavelength (nm)	Bandwidth (nm)
1	440	25
2	500	20
3	530	15
4	570	12
5	610	10
6	670	12
7	740	15
8	780	20
9	840	25
10	900	30
11	950	50
12	1000	50

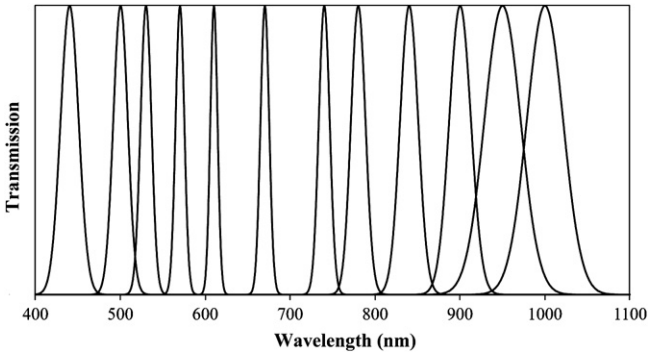

Fig. 16. Modelled transmission profiles for the proposed ExoMars PanCam geology filter set.

lower QE of the Star 1000 in this region as compared to the CCD detectors used for previous missions.

It should be noted that in the exposure time model, the transmission of optical elements in the camera other than the filters were not considered. For many space applications, radiation hardened optical glass is used for optical elements to reduce radiation induced damage and yellowing in the glass. Such glass usually contains Cerium to provide the radiation resistance properties, but this also causes some yellowing of the glass and so can significantly reduce the transmission at short wavelength. Some basic simulations have indicated that if radiation hardened optical glass were used for the lenses, light transmission at 440 nm could be reduced by 75%, increasing exposure time by a factor of 4 for this filter. For this reason it may be necessary to re-optimise the bandwidths of some filters once the specification of the optical elements are known.

4. Conclusions

4.1. Recommendation of the "FERRIC" filter set

The correct identification of putative Martian palaeoenvironments using in situ PanCam data, including multispectral data, will be imperative to site selection and identification of drilling targets. Maximising information return using limited resources (in this case, sampling just 12 wavelengths in the Vis–NIR) will further the ability of the PanCam instrument to achieve this goal.

Testing of the alternative filter sets on both mineral and rock spectral data has shown an improved performance of the new filter sets FERRIC, PHYL, and ALLFe, and also of the earlier devised (and more generic) filter set F2-12. Whilst filter sets FERRIC and PHYL are highly specific with regards to their design, testing on minerals and rock targets has shown them to capture spectral features that they were not in theory optimised to detect. Conversely, the other filter sets (SULPH, MAFIC, and HYDRA) often poorly represented mineral and rock spectra. HYDRA especially was formulated based on mineral spectral with very few absorption features other than specific hydration absorptions in the NIR, and it is unsurprising this filter set performed the worst. Ideally, significantly more work would further clarify the performance of the best filter sets (especially in the case of FERRIC and PHYL), particularly with regard to the discrimination of a far wider sample set. However, the basic ability of FERRIC to identify nearly all the minerals tested, along with being designed to capture the main absorption bands within the PanCam spectral range, results in this filter set being recommended as the wavelengths of the geological filters for ExoMars.

4.2. Bandwidth selection

The effects of both bandwidth and exposure time on the accuracy with which a spectrum can be reproduced have been considered. A set of bandwidths which will allow the camera to work effectively with as short an exposure time as possible whilst keeping the error low has been proposed. In spite of the fact that some of the bandwidths (50 nm) are wider than have been used in the PanCam instruments on previous missions, simulations indicate that this will not have a detrimental effect in performance of the filter set, with the error score still being lower for the FERRIC filter set than those calculated for the other missions.

4.3. Wider implications

One of the many scientific roles PanCam data will be required for is the remote selection of rock/soil or outcrop targets proximal to the rover. The ability of the FERRIC filter set to reproduce the reflectance spectral profile (between 440 and 1000 nm) of nearly all the hydrated minerals, iron oxides, and mafic silicates tested demonstrates that the multispectral aspect of PanCam imaging is well equipped to deal with the Martian surface geology. Taking some of the MSL landing site candidates as example terrains, mineralogical assemblages that the ExoMars rover may encounter include:

- Fe-smectite/nontronite+mono/poly-hydrated sulphate+haematite+olivine+pyroxene (*Gale Crater*, Milliken et al., 2010).
- Fe/Mg phyllosilicates+high Ca-pyroxene (clinopyroxene)+olivine+other hydrated minerals (*Eberswalde crater*, McKeown and Rice, 2011).
- Fe/Mg smectites+hydrated silica+montmorillonite+kaolinite+haematite (*Mawrth Vallis*, Wray et al., 2008).
- Fe/Mg smectites+chlorite+prehnite+serpentine+kaolinite+illite/muscovite opaline silica+analcime+magnesite+olivine (*Nili Fossae*, Ehlmann et al., 2009).

The FERRIC filter wavelengths are well placed to capture the spectral features of these mineral species, with the exception of the small 630 nm absorption in olivine. As mentioned, multispectral imaging with the PanCam filters is not necessarily going to provide identification of specific mineral species. However, as seen with the candidate MSL landing sites, the Martian surface geology is diverse, and the increased ability of the FERRIC filter set to capture both absorption bands and subtle spectral morphologies mean the ExoMars PanCam will be optimised to distinguish between compositional units observable within outcrops.

A downside to changing the geology filters on ExoMars from those used on the MERs will be that any ExoMars PanCam results will not be *directly* comparable to those of MER. Likewise, there has been several years of MER Pancam data processing/interpreting

experience that will not be completely applicable to ExoMars PanCam data if the filters change (e.g., identical band parameters and stretching cannot always be employed). However, these new geology filters will provide different observations to the MERs, which ultimately will expand our in-situ multispectral observations of Martian terrain. Additionally, new band parameters and ratios can be explored, and may lead to new discoveries that would otherwise be missed by the old filters.

Acknowledgements

This work is funded by the Leverhulme Trust and the UK Science and Technology Facilities Council (STFC), who are the lead funding agency for the development of the ExoMars Panoramic Camera. Additional support for this work was provided by HEFCW through the Centre for Advanced Functional Materials and Devices (CAFMaD).

Appendix A. Supporting information

Supplementary data associated with this article can be found in the online version at http://dx.doi.org/10.1016/j.pss.2012.07.009.

References

Allen, C.C., Albert, F.G., Chafetz, H.S., Combie, J., Graham, C.R., Kieft, T.L., Kivett, S.J., McKay, D.S., Steele, A., Taunton, A.E., Taylor, M.R., Thomas-Keprta, K.L., Westall, F., 2000. Microscopic physical biomarkers in carbonate hot springs: implications in the search for life on Mars. Icarus 147, 49–67.

Aubrey, A., Cleaves, H.J., Chalmers, J.H., Skelley, A.M., Mathies, R.A., Grunthaner, F., Ehrenfreund, P., Bada, J.L., 2006. Sulfate minerals and organic compounds on Mars. Geology 34, 357–360.

Baldridge, A.M., Hook, S.J., Grove, C.I., Rivera, G., 2009. The ASTER spectral library version 2.0. Remote sensing of environment. Remote Sensing of Environment 113, 711–715.

Bandfield, J.L., 2002. Global mineral distributions on Mars. Journal of Geophysical Research 107, E6, , http://dx.doi.org/10.1029/2001JE001510.

Bell, J.F., Squyres, S.W., Herkenhoff, K.E., Maki, J.N., Arneson, H.M., Brown, D., Collins, S.A., Dingizian, A., Elliot, S.T., Hagerott, E.C., Hayes, A.G., Johnson, M.J., Johnson, J.R., Joseph, J., Kinch, K., Lemmon, M.T., Morris, R.V., Scherr, L., Schwochert, M., Shepard, M.K., Smith, G.H., Sohl-Dickstein, J.N., Sullivan, R.J., Sullivan, W.T., Wadsworth, M., 2003. Mars Exploration Rover Athena Panoramic Camera (Pancam) investigation. Journal of Geophysical Research 108 (E12), 8063.

Bell, J.F., Squyres, S.W., Arvidson, R.E., Arneson, H.M., Bass, D., Blaney, D., Cabrol, N., Calvin, W., Farmer, J., Farrand, W.H., Goetz, W., Golombek, M., Grant, J.A., Greeley, R., Guinness, E., Hayes, A.G., Hubbard, M.Y.H., Herkenhoff, K.E., Johnson, M.J., Johnson, J.R., Joseph, J., Kinch, K.M., Lemmon, M.T., Li, R., Madsen, M.B., Maki, J.N., Malin, M., McCartney, E., McLennan, S., McSween Jr., H.Y., Ming, D.W., Moersch, J.E., Morris, R.V., Noe Dobrea, E.Z., Parker, T.J., Proton, J., Rice Jr., J.W., Seelos, F., Soderblom, J., Soderblom, L.A., Sohl-Dickstein, J.N., Sullivan, R.J., Wolff, M.J., Wang, A., 2004. Pancam multispectral imaging results from the Spirit rover at Gusev Crater. Science 305, 800–806.

Bibring, J.-P., Langevin, Y., Mustard, J.F., Poulet, F., Arvidson, R., Gendrin, A., Gondet, B., Mangold, N., Pinet, P., Forget, F., 2006. Global mineralogical and aqueous Mars history derived from the OMEGA/Mars Express data. Science 312, 400–404.

Bibring, J.-P., et al., 2007. Coupled ferric oxides and sulfates on the Martian surface. Science 317, 1206–1210.

Bishop, J.L., Dobrea, E.Z.D., McKeown, N., Parente, K., Ehlmann, M., Michalski, B.L., Milliken, J.R., Poulet, R.E., Swayze, D., Mustard, G.A., Murchie, J.F., BibringJ.-P., S.L., 2008. Phyllosilicate diversity and past aqueous activity revealed at Mawrth Vallis, Mars. Science 321, 830–833.

Bishop, J.L., Schiffman, P., Southard, R., 2002. Geochemical and mineralogical analyses of palagonitic tuffs and altered rinds of pillow basalts in Iceland and applications to Mars. In: Smellie, J.L., Chapman, M.G. (Eds.), Volcano-Ice Interaction on Earth and Mars, 202. Geological Society, London, pp. 371–392In: Smellie, J.L., Chapman, M.G. (Eds.), Volcano-Ice Interaction on Earth and Mars, 202. Geological Society, London, pp. 371–392 , Special Publications.

Boynton, W.V., Ming, D.W., Kounaves, S.P., Young, S.M.M., Arvidson, R.E., Hecht, M.H., Hoffman, J., Niles, P.B., Hamara, D.K., Quinn, R.C., Smith, P.H., Sutter, B., Catling, D.C., Morris, R.V., 2009. Evidence of calcium carbonate at the Mars Phoenix landing site. Science 325, 61–64.

Chevrier, V., Mathe, P.E., 2007. Mineralogy and evolution of the surface of Mars: a review. Planetary and Space Science 55, 289–314.

Clark, R.N., Swayze, G.A., Wise, R., Livo, E., Hoefen, T., Kokaly, R., Sutley, S.J., 2007. USGS digital spectral library splib06a: U.S. Geological Survey. Digital Data Series, 231.

Clark, R.N., Swayze, G.A., Gallagher, A.G., King, T.V.V., Calvin, W.M., 1993. The U. S. Geological Survey, Digital Spectral Library: Version 1: 0.2 to 3.0 μm. U.S. Geological Survey Open File Report, 93–592.

Cousins, C.R., Griffiths, A.D., Crawford, I.A., Prosser, B.J., Storrie-Lombardi, M.C., Davis, L.E., Gunn, M., Coates, A.J., Jones, A.P., Ward, J.M., 2010. Astrobiological considerations for the selection of the geological filters on the ExoMars PanCam instrument. Astrobiology 10, 933–951.

Dartnell, L.R., Storrie-Lombardi, M.C., Ward, J.M., 2010. Complete fluorescence fingerprints of extremophilic and photosynthetic microbes. International Journal of Astrobiology 9, 245–257.

Ehlmann, B.L., Mustard, J.F., Murchie, S.L., Bibring, J.-P., Meunier, A., Frawman, A.A., Langevin, Y., 2011. Subsurface water and clay mineral formation during the early history of Mars. Nature 479, 53–60.

Ehlmann, B.L., Mustard, J.F., Swayze, G.A., Clark, R.N., Bishop, J.L., Poulet, F., Des Marais, D.J., Roach, L.H., Milliken, R.E., Wray, J.J., Barnouin-Jha, O., Murchie, S.L., 2009. Identification of hydrated silicate minerals on Mars using MRO-CRISM: Geologic context near Nili Fossae and implications for aqueous alteration. Journal of Geophysical Research 114, E00D08, http://dx.doi.org/10.1029/2009JE003339.

Ehlmann, B.L., Mustard, J.F., Murchie, S.L., Poulet, F., Bishop, J.L., Brown, A.J., Calvin, W.M., Clark, R.N., Des Marais, D.J., Milliken, R.E., Roach, L.H., Roush, T.L., Swayze, G.A., Wray, J.J., 2008a. Orbital identification of carbonate-bearing rocks on Mars. Science 322, 1928–1832.

Ehlmann, B.L., Mustard, J.F., Fassett, C.I., Schon, S.C., Head, J.W., Des Marais, D.J., Grant, J.A., Murchie, S.L., 2008b. Clay minerals in delta deposits and organic preservation potential on Mars. Nature Geoscience 1, 355–358.

Farrand, W.H., et al., 2009. Discovery of jarosite within the Mawrth Vallis region of Mars. Icarus 204, 478–488.

Farrand, W.H., Bell, J.F., Johnson, J.R., Arvidson, R.E., Crumpler, L.S., Hurowitz, J.A., Schroder, C., 2008. Rock spectral classes observed by the Spirit Rover's Pancam on the Gusev Crater Plains and in the Columbia Hills. Journal of Geophysical Research 113, E12S38, http://dx.doi.org/10.1029/2008JE003237.

Farrand, W.H., Bell, J.F., Johnson, J.R., Jolliff, B.L., Knoll, A.H., McLennan, S.M., Squyres, S.W., Calvin, W.M., Grotzinger, J.P., Morris, R.V., Soderblom, J., Thompson, S.D., Watters, W.A., Yen, A.S., 2007. Visible and near-infrared multispectral analysis of rocks at Meridiani Planum, Mars, by the Mars Exploration Rover Opportunity. Journal of Geophysical Research 112, E06S02.

Farrand, W.H., Bell III, J.F., Johnson, J.R., Squyres, S.W., Soderblom, J., Ming, D.W., 2006. Spectral variability among rocks in visible and near-infrared multispectral Pancam data collected at Gusev crater: examinations using spectral mixture analysis and related techniques. Journal of Geophysical Research 111, E02S15, http://dx.doi.org/10.1029/2005JE002495.

Gendrin, A., Mangold, N., Bibring, J.-P., Langevin, Y., Gondet, B., Poulet, F., Bonello, G., Quantin, C., Mustard, J., Arvidson, R., LeMouelic, S., 2005. Sulfates in martian layered terrains: the OMEGA/Mars express view. Science 307 (2005), 1587–1591.

Ghaemi, F.T., 2009. Design and fabrication of lenses for the color science cameras aboard the Mars Science Laboratory rover. Optical Engineering 48, 103002, http://dx.doi.org/10.1117/1.3251343.

Griffiths, A.D., Coates, A.J., Josset, J.-L., Paar, G., Hofmann, B., Pullan, D., Ruffer, P., Sims, M.R., Pillinger, C.T., 2005. The Beagle 2 stereo camera system. Planetary and Space Science 53, 1466–1482.

Griffiths, A.D., Coates, A.J., Jaumann, R., Michaelis, H., Paar, G., Barnes, D., Josset, J.-L., 2006. the PanCam Team., 2006. Context for the ESA ExoMars rover: the Panoramic Camera (PanCam) instrument. International Journal of Astrobiology 5, 269–275.

Hausrath, E.M., Navarre-Sitchler, A.K., Sak, P.B., Steefal, C.I., Brantley, S.L., 2008a. Basalt weathering rates on Earth and the duration of liquid water on the plains of Gusev Crater, Mars. Geology 36, 67–70.

Hausrath, E.M., Treiman, A.H., Vicenzi, E., Bish, D.L., Blake, D., Sarrazin, P., Hoehler, T., Midtandal, I., Steele, A., Brandley, S.L., 2008b. Short- and long-term olivine weathering in Svalbard: implications for Mars. Astrobiology 8, 1079–1092.

Hecht, M.H., Kounaves, S.P., Quinn, R.C., West, S.J., Young, S.M.M., Ming, D.W., Catling, D.C., Clark, B.C., Boynton, W.V., Hoffman, J., DeFlores, L.P., Gospodinova, K., Kapit, J., Smith, P.H., 2009. Detection of perchlorate and the soluble chemistry of martian soil at the Phoenix lander site. Science 325, 64–67.

Johnson, J.R., Bell, J.F., Cloutis, E., Staid, M., Farrand, W.H., McCoy, T., Rice, M., Wang, A., Yen, A., 2007. Mineralogic constraints on sulfur-rich soils from Pancam spectra at Gusev crater, Mars. Geophysical Research Letters 34, L13202, http://dx.doi.org/10.1029/2007GL029894.

Langevin, Y., Poulet, F., Bibring, J.-P., Gondet, B., 2005. Sulfates in the north polar region of Mars detected by OMEGA/Mars Express. Science 307, 1584–1586.

Lemmon, M.T., Smith, P., Shinohara, C., Tanner, R., Woida, P., Shaw, A., Hughes, J., Reynolds, R., Woida, R., Penegor, J., Oquest, C., Hviid, S.F., Madsen, M.B., Olsen, M., Leer, K., Drube, L., Morris, R.V., Britt, D. (2008). The Pheonix surface stereo imager (SSI) investigation. Lunar and Planetary Science XXXIX (abstract 2156).

Loizeau, D., Mangold, N., Poulet, F., Bibring, J.-P., Gendrin, A., Ansan, V., Gomez, C., Gondet, B., Langebin, Y., Masson, P., Neukum, G., 2007. Phyllosilicates in the Mawrth Vallis region of Mars. Journal of Geophysical Research 112, E08S08.

McKeown, N.K., Rice, M.S. (2011) Detailed mineralogy of Eberswalde crater. 42nd Lunar and Planetary Science Conference, Abstract 2450.

McSween, H.Y., Taylor, G.J., Wyatt, M.B., 2009. Elemental Composition of the Martian Crust. Science 324, 736–739.
Michalski, J.R., Niles, P.B., 2010. Deep crustal carbonate rocks exposed by meteor impact on Mars. Nature Geoscience 3, 751–755.
Milam, K.A., McSween, H.Y., Moersch, J., Christensen, P.R., 2010. Distribution and variation of plagioclaste compositions on Mars. Journal of Geophysical Research 115, E09004, http://dx.doi.org/10.1029/2009JE003495.
Milliken, R.E., Grotzinger, J.P., Thomson, B.J., 2010. Paleoclimate of Mars as captured by the stratigraphic record in Gale Crater. Geophysical Research Letters 37, L04201, http://dx.doi.org/10.1029/2009GL04187.
Milliken, R.E., Swayze, G.G., Arvidson, R.E., Bishop, J.L., Clark, R.N., Ehlmann, B.L., Green, R.O., Grotzinger, J.P., 2008. Opaline silica in young deposits on Mars. Geology 36, 847–850.
Morris, R.V., Klingelhotder, G., Schroder, C., Rodionov, S.D., Yen, A., Ming, D.W., de Souza, P.A., Fleischer, I., Wdowiak, T., Gellert, R., Bernhardt, B., Evlanov, E.N., Zubkov, B., Foh, J., Bonnes, U., Kankeleit, E., Gutlich, P., Renz, F., Squyres, S.W., Arvidson, R.E., 2006. Mossbauer mineralogy of rock, soil, and dust at Gusev crater, Mars: Spirit's journey through weakly altered olivine basalt on the plains and pervasively altered basalt in the Columbia Hills. Journal of Geophysical Research 111, E02S13, http://dx.doi.org/10.1029/2005JE002584.
Morris, R.V., Golden, D.C., Bell, J.F., Shelfer, T.D., Scheinost, A.C., Hinman, N.W., Furniss, G., Mertzman, S.A., Bishop, J.L., Ming, D.W., Allen, C.C., Britt, D.T., 2000. Mineralogy, composition, and alteration of Mars Pathfinder rocks and soils: evidence from multispectral, elemental, and magnetic data on terrestrial analogue, SNC meteorite, and Pathfinder samples. Journal of Geophysical Research 105, 1757–1817.
Murchie, S.L., et al., 2009. A synthesis of Martian aqueous mineralogy after one Mars year of observations from the Mars Reconnaissance Orbiter. Journal of Geophysical Research 114, E00D06, http://dx.doi.org/10.1029/2009JE003342.
Mustard, J.F., Murchie, S.L., Pelkey, S.M., Ehlmann, B.L., Milliken, R.E., Grant, J.A., Bibring, J.-P., Poulet, F., Bishop, J., Noe Dobrea, E.N., Roach, L., Seelos, F., Arvidson, R.E., Wiseman, S., Green, R., Hash, C., Humm, D., Malaret, E., McGovern, J.A., Seelos, K., Clancy, T., Clark, R., Marais, D.D., Izenberg, N., Knudson, A., Langevin, Y., Martin, T., McGuire, P., Morris, R., Robinson, M., Roush, T., Smith, M., Swayze, G., Taylor, H., Titus, T., Wolff, M., 2008. Hydrated silicate minerals on Mars observed by the Mars Reconnaissance Orbiter CRISM instrument. Nature 454, 305–309.
Osterloo, M.M., Hamilton, V.E., Bandfield, J.L., Glotch, T.D., Baldridge, A.M., Christensen, P.R., Tornabene, L.L., Anderson, F.S., 2008. Chloride-bearing materials in the southern highlands of Mars. Science 319L, 1651–1654.
Poulet, F., Bibring, J.-P., Mustard, J.F., Gendrin, A., Mangold, N., Langevin, Y., Arvidson, R.E., Gondet, B., Gomez, C., 2005. Phyllosilicates on Mars and implications for early Martian climate. Nature 438, 623–627.
Preston, L.J., Shuster, J., Fernandez-Remolar, D., Banerjee, N.R., Osinski, G.R., Southam, G., 2011. The preservation and degradation of filamentous bacteria and biomolecules within iron oxide deposits at Rio Tinto, Spain. Geobiology 9, 233–249.
Rice, M.S., Bell, J.F., Cloutis, E.A., Wang, A., Ruff, S.W., Craig, M.A., Bailey, D.R., Johnson, J.R., de Souza Jr., P.A., Farrand, W.H., 2010. Silica-rich deposits and hydrated minerals at Gusev Crater, Mars: Vis–NIR spectral characterization and regional mapping. Icarus 205, 375–395.
Schmidt, M.E., Farrand, W.H., Johnson, J.R., Schroder, C., Hurowitx, J.A., McCoy, T.J., Ruff, S.W., Arvidson, R.E., Des Marais, D.J., Lewis, K.W., Ming, D.W., Squyres, S.W., de Souza, P.A., 2009. Spectral, mineralogical, and geochemical variations across Home Plate, Gusev Crater, Mars indicate high and low temperature alteration. Earth and Planetary Science Letters 281, 258–266.
Smith, P.H., Tomasko, M.G., Britt, D., Crowe, D.G., Reid, R., Keller, H.U., Thomas, N., Gliem, F., Rueffer, P., Sullivan, R., Greely, R., Knudsen, J.M., Madsen, B., Gunnlaugsson, H.P., Hviid, S.F., Goetz, W., Soderblom, L.A., Gaddis, L., Kirk, R., 1997b. The imager for Mars Pathfinder experiment. Journal of Geophysical Research 102, 4003–4025.
Smith, P.H., Tomasko, M.G., Britt, D., Crowe, D.G., Reid, R., Keller, H.U., Thomas, N., Gliem, F., Rueffer, P., Sullivan, R., Greely, R., Knudsen, J.M., Madsen, B., Gunnlaugsson, H.P., Hviid, S.F., Goetz, W., Soderblom, L.A., Gaddis, L., Kirk, R., 1997a. The imager for Mars Pathfinder experiment. Journal of Geophysical Research 102, 4003–4025.
Squyres, S.W., Arvidson, R.E., Ruff, S., Gellert, R., Morris, R.V., Ming, D.W., Crumpler, L., Farmer, J.D., Des Marais, D.J., Yen, A., McLennan, S.M., Calvin, W., Bell, J.F., Clark, B.C., Wang, A., McCoy, T.J., Schmidt, M.E., de Souza, P.A., 2008. Detection of Si-rich deposits on Mars. Science 320, 1063–1067.
Squyres, S.W., et al., 2004. In-situ evidence for an ancient aqueous environment at Meridiani Planum. Science 306, 1709–1714.
Storrie-Lombardi, M.C., Muller, J.-P., Fisk, M.R., Cousins, C., Sattler, B., Griffiths, A.D., Coates, A.J., 2009. Laser-induced fluorescence emission (L.I.F.E.): search for Mars organics with a UV-Enhanced PanCam. Astrobiology 9, 953–964.
Stroncik, N.A., Schmincke, H.-U., 2002. Palagonite-a review. International Journal of Earth Sciences 91, 680–697.
Uwaerts, D. (2006) STAR 1000 Detailed Specification, Fill Factory image sensors.
Warner, N.H., Farmer, J.D., 2010. Subglacial hydrothermal alteration minerals in jökulhlaup deposits of Southern Iceland, with implications for detecting past or present habitable environments on Mars. Astrobiology 10, 523–547.
Weider, S.Z., Swinyard, B.M., Kellett, B.J., Howe, C.J., Joy, K.H., Crawford, I.A., Gow, J., Smith, D.R., 2011. Planetary X-ray fluorescence analogue laboratory experiments and an elemental abundance algorithm for C1XS. Planetary and Space Science 59, 1393–1407.
Weitz, C.M., Bishop, J.L., Thollot, P., Mangold, N., Roach, L.H., 2011. Diverse mineralogies in two troughs of Noctis Labyrinthus, Mars. Geology 39, 899–902.
Wray, J.J., Murchie, S.L., Squyres, S.W., Seelos, F.P., Tornabene, L.L., 2009. Diverse aqueous environments on ancient Mars revealed in the southern highlands. Geology 37, 1043–1046.
Wray, J.J., Ehlmann, B.L., Squyres, S.W., Mustard, J.F., Kirk, R.L., 2008. Compositional stratigraphy of clay-bearing layered deposits at Mawrth Vallis, Mars. Geophysical Research Letters 35, L12202, http://dx.doi.org/10.1029/2008GL034385.